Monthly Notices
of the
ROYAL ASTRONOMICAL SOCIETY

MNRAS **488,** 1597–1617 (2019)
Advance Access publication 2019 July 4

doi:10.1093/mnras/stz1829

GASP – XX. From the loose spatially resolved to the tight global SFR–mass relation in local spiral galaxies

Benedetta Vulcani [1]★ Bianca M. Poggianti,[1] Alessia Moretti [1] Andrea Franchetto,[1,2] Marco Gullieuszik,[1] Jacopo Fritz [3] Daniela Bettoni,[1] Stephanie Tonnesen,[4] Mario Radovich [1] Yara L. Jaffé [5] Sean McGee,[6] Callum Bellhouse [6] and Giovanni Fasano[1]

[1]*INAF – Osservatorio astronomico di Padova, Vicolo Osservatorio 5, I-35122 Padova, Italy*
[2]*Dipartimento di Fisica & Astronomia 'Galileo Galilei', Università di Padova, vicolo dell' Osservatorio 3, I-35122 Padova, Italy*
[3]*Instituto de Radioastronomía y Astrofísica, UNAM, Campus Morelia, A.P. 3-72, C.P. 58089, Mexico*
[4]*Center for Computational Astrophysics, Flatiron Institute, 162 5th Ave, New York, NY 10010, USA*
[5]*Instituto de Física y Astronomía, Universidad de Valparaíso, Avda. Gran Bretaña, 1111 Valparaíso, Chile*
[6]*School of Physics and Astronomy, University of Birmingham, Edgbaston, Birmingham, B15 2TT UK*

Accepted 2019 June 28. Received 2019 June 28; in original form 2019 April 9

ABSTRACT

Exploiting the sample of 30 local star-forming, undisturbed late-type galaxies in different environments drawn from the GAs Stripping Phenomena in galaxies with MUSE (GASP), we investigate the spatially resolved star formation rate–mass ($\Sigma_{\rm SFR}$–Σ_*) relation. Our analysis includes also the galaxy outskirts (up to >4 effective radii, $r_{\rm e}$), a regime poorly explored by other Integral Field Spectrograph surveys. Our observational strategy allows us to detect Hα out to more than 2.7$r_{\rm e}$ for 75 per cent of the sample. Considering all galaxies together, the correlation between the $\Sigma_{\rm SFR}$ and Σ_* is quite broad, with a scatter of 0.3 dex. It gets steeper and shifts to higher Σ_* values when external spaxels are excluded and moving from less to more massive galaxies. The broadness of the overall relation suggests galaxy-by-galaxy variations. Indeed, each object is characterized by a distinct $\Sigma_{\rm SFR}$ –Σ_* relation and in some cases the correlation is very loose. The scatter of the relation mainly arises from the existence of bright off-centre star-forming knots whose $\Sigma_{\rm SFR}$–Σ_* relation is systematically broader than that of the diffuse component. The $\Sigma_{\rm SFR}$–$\Sigma_{\rm tot\,gas}$ (total gas surface density) relation is as broad as the $\Sigma_{\rm SFR}$–Σ_* relation, indicating that the surface gas density is not a primary driver of the relation. Even though a large galaxy-by-galaxy variation exists, mean $\Sigma_{\rm SFR}$ and Σ_* values vary of at most 0.7 dex across galaxies. We investigate the relationship between the local and global SFR–M_* relation, finding that the latter is driven by the existence of the size–mass relation.

Key words: galaxies: evolution – galaxies: spiral – galaxies: star formation.

1 INTRODUCTION

The star formation rate (SFR)–mass relation (M_*) is one of the most studied relations in astrophysics (e.g. Brinchmann et al. 2004; Salim et al. 2007; Noeske et al. 2007a, b). It shows how tightly a galaxy's SFR and its total stellar mass are related, at any redshift, for star-forming galaxies (star-forming main sequence, SFMS). Higher stellar mass systems undergo more intense star formation activity than lower mass systems. At all redshifts, the dispersion of the correlation is only 0.2–0.3 dex in SFR for a fixed mass and the slope is somewhat smaller than unity, implying that the relative rate at which stars form in galaxies, i.e. the specific star formation rate (SSFR), declines weakly with increasing galaxy mass (Salim et al. 2007; Schiminovich et al. 2007). From $z = 0$ to high redshift the normalization increases to higher values: by $z \sim 2$ at a fixed stellar mass SFRs are higher by a factor of ∼20 (e.g. Daddi et al. 2007; Noeske et al. 2007a; Vulcani et al. 2010; Elbaz et al. 2011; Whitaker et al. 2012; Speagle et al. 2014; Schreiber et al. 2015; Barro et al. 2017).

The existence of such relation points to a scenario where galaxies form through secular processes rather than stochastic merger-driven star-forming episodes. Universal laws seem to govern their evolution throughout cosmological time and across many different environments. Galaxies evolve along the SFMS, increasing in mass through the accretion of cold gas through mergers and/or from the cosmic web, until the supply of gas is shut off, most likely when a

★ E-mail: benedetta.vulcani@inaf.it

© 2019 The Author(s)
Published by Oxford University Press on behalf of the Royal Astronomical Society

Downloaded from https://academic.oup.com/mnras/article/488/2/1597/5528330 by CIS Psicologia Biblioteca F.Metelli - Universita degli Studi di Padova user on 03 November 2020

critical mass is reached (Cattaneo et al. 2006). Star formation is thus interrupted, and the galaxy moves to the red sequence, where it may further grow in mass and size through minor mergers (e.g. Faber et al. 2007; Lilly et al. 2013). The quenching phase is critical in the life of a galaxy, none the less, the conditions leading the galaxy quenching are still obscure.

A great limitation to the comprehension of the connection between SFR and M_* is that most studies consider galaxies as a whole, with integrated observations that do not distinguish among the morphological components, or that only partially cover the galaxies and are thus subject to aperture effects. A step forward is to characterize the relation on smaller scales, using spatially resolved data.

If the relation between star formation and mass still held on small scales, it would suggest that the global SFR–M_* relation is primarily the outcome of the local correlation and the mechanism that drives the star formation activity with respect to the stellar mass could be universal across various physical scales, similarly to the Kennicutt–Schmidt relation (Kennicutt 1998b) between the SFR surface density ($\Sigma_{\rm SFR}$) and the cold gas surface density that has been found to hold both locally (e.g. Bigiel et al. 2008) and globally. The opposite is indeed unreasonable, as it seems rather fine-tuned that a mechanism acting on global scales affects both the surface mass density (Σ_*) and $\Sigma_{\rm SFR}$ exactly in the same way, without a local process being involved or that a process reverts to the mean when averaged over large volumes.

On the other hand, the lack of a correlation between these spatially resolved quantities would suggest a galaxy-wide process that regulates the SFR of galaxies as a whole.

Outside our Galaxy, spatially resolved properties have been investigated for M31 (Viaene et al. 2014), who performed SED fitting of a panchromatic dataset, covering UV to submm wavelengths at a physical resolution of 140 × 600 pc. They found that regions of higher Σ_* tend to host less star formation, suggesting an internal downsizing process in star formation, in which the regions of highest stellar density have already stopped forming stars. In addition, star formation at small scales has a weak dependence on the stellar mass: small-scale environments characterized by different stellar masses can be associated with very different levels of star formation.

An attempt to study the spatially resolved SFMS relation in local ($0.01 < z < 0.02$) massive disc galaxies using photometric data was performed by Abdurro'uf & Masayuki (2017), who combined seven bands imaging data from Galaxy Evolution Explorer and Sloan Digital Sky Survey fitting the spatially resolved SED of a galaxy with a set of model photometric SEDs using a Bayesian statistics approach. They showed that the relation is almost linear and presents a bending at $\Sigma_* = 3.1 \times 10^7\,{\rm M}_\odot\,{\rm kpc}^{-2}$. The same authors also applied the same technique at higher redshift, finding overall similar results (Abdurro'uf & Masayuki 2018). Exploiting 10-band photometry from the UV to the near-infrared at *HST* resolution, Morselli et al. (2019) derived spatially resolved maps of stellar masses and SFRs, finding that the star formation activity is centrally enhanced in galaxies above the SFMS and centrally suppressed below it. The level of suppression correlates with the distance from the SFMS. They concluded that the presence of the bulge plays an important role: at a fixed stellar mass, bulge-dominated galaxies are preferentially located below the SFMS, while disk-like galaxies with low Sersic indexes are preferentially located on the upper envelope of the SFMS. The suppression of star formation activity in the central region of galaxies below the SFMS points to an inside-out quenching scenario, as star formation is still ongoing in the outer regions. The importance of separating the contribution of bulges and disks has also been emphasized by Abramson et al. (2014), who argued that re-normalizing the SFR by disc stellar mass, the star formation efficiency (SFE) does not depend anymore on galaxy mass for star-forming discs, In contrast, Willett et al. (2015) found no statistically significant difference in the SFR–M_* relations in a wide range of nearby morphological subtypes of star-forming disc galaxies, suggesting that these systems are strongly self-regulated.

The great step forward to the comprehension of the connection between SFR and M_* is due to the advent of the Integral Field Spectroscopy (IFS) surveys, such as ATLAS3D (Cappellari et al. 2011)[1], CALIFA (Sánchez et al. 2012; Husemann et al. 2013; García-Benito et al. 2015), SAMI (Bryant et al. 2015), and MaNGA (Bundy et al. 2015), that have been designed to better understand the star formation and quenching in galaxies and that should help disentangle the contributions of different parameters to the SFR–M_* relation, in the local Universe. These surveys observed from ∼100 to 10 000 galaxies, with a spatial coverage ranging from at most 1–3 effective radii ($r_{\rm e}$). A complete comparison among the different surveys is given in table 3 of Bundy et al. (2015).

All the largest IFU surveys have found overall concordant results, that can be summarized as follows. In nearby galaxies, Σ_* and $\Sigma_{\rm SFR}$ for regions where star formation dominates the ionization constitute a tight correlation (Rosales-Ortega et al. 2012; Sánchez 2013; Liu et al. 2018; Pan et al. 2018; Erroz-Ferrer et al. 2019). Hall et al. (2018) have found that the slopes and zero-points of the different SFMS probed at different spatial resolution scales ranging from 0.05 to 10 kpc remain essentially the same. Also the scatter at each resolution scale is relatively constant out to 0.5–1 kpc, dropping slightly beyond that range (see also Kruijssen & Longmore 2014). This correlation is invariant to changes in global properties, such as inclination, total stellar mass, local environment, H I mass, redshift (Cano-Díaz et al. 2016; Ellison et al. 2018; Hall et al. 2018, but see Medling et al. 2018 for a dependence of the SFR distribution on galaxy local number density).

Cano-Díaz et al. (2016) exploiting CALIFA data and Hsieh et al. (2017) investigating MaNGA data have also shown that the slope and dispersion of this local SFMS are similar to those of the global SFR–M_* relation (see also Hall et al. 2018). This result has also been shown to hold at higher redshift (Wuyts et al. 2013; Magdis et al. 2016). The remarkable agreement between the local and global SFR and M_* relations suggests that the global main sequence may originate from a more fundamental relation on small scales and that the SFR is controlled by the amount of old stars locally (Hsieh et al. 2017).

The scatter of the $\Sigma_{\rm SFR}$–Σ_* relation is strongly related to Hubble type (González Delgado et al. 2016), with the relation becoming less tight when early-type galaxies are considered in the sample. In fact, a subpopulation of non-passive early-type galaxies exists (Sarzi et al. 2010; Medling et al. 2018) and these are preferentially located below the SFMS. According to Medling et al. (2018), the presence of a bulge plays only a marginal role: some galaxies with bulges continue their star formation exactly as late-type spirals would. On the other hand, González Delgado et al. (2016) and Maragkoudakis et al. (2017) found that galaxies with higher bulge fractions tend to exhibit lower SFR for their Σ_*. In M31, Viaene et al. (2014) found that the bulk of stars formed at early epochs in the bulge,

[1]Note that because of its focus on early-type galaxies, ATLAS3D essentially avoids star-forming systems, it is not an ideal sample to study the SFMS (McDermid et al. 2015).

Downloaded from https://academic.oup.com/mnras/article/488/2/1597/5528330 by CIS Psicologia Biblioteca F.Metelli - Universita degli Studi di Padova user on 03 November 2020

and the more recent star formation happens at larger galactocentric distances (i.e. >3 kpc).

The clear role of Hubble type in defining the offset around the overall Σ_{SFR}–Σ_* relation suggests that some global morphology-related property modulates the local Σ_{SFR} , such as the gas content (Roberts & Haynes 1994; Tacconi et al. 2013).

In spite of the many works focused on the spatially resolved Σ_{SFR}–Σ_* relation, no study has focused on the relation separately for bright H II regions and diffuse component. Indeed, the two components give different information about the gas-stellar cycle. H II regions are photoionized by massive young stars formed recently; the diffuse component (also known as warm ionized medium, WIM) is a warm ($\sim 10^4$ K), ionized, low-density (0.1 cm^{-3}) gas between H II regions typically with low-ionization parameter that can extend 1 kpc or more above the disk plane (Mathis 2000; Haffner et al. 2009, and references therein). This gas component is most likely ionized by stars (O, B, and hot evolved stars) in the disc whose Lyman continuum photons travel large path lengths (Mathis 1986, 2000; Domgorgen & Mathis 1994; Sembach et al. 2000; Wood & Mathis 2004; Wood et al. 2010). Understanding if the two components follow similar Σ_{SFR}–Σ_* relations is thought important to understand their physics. Recently, a lot of effort is being put to characterize the metallicity of this diffuse component (e.g. Yan 2018; Kumari et al. 2019). Erroz-Ferrer et al. (2019) have contrasted the metallicity of the H II region and the diffuse component, finding that the former have on average metallicities 0.1 dex higher than the latter.

In this paper we present the analysis of the spatially resolved SFR–M_* relation for 30 undisturbed late-type galaxies in different environments drawn from the GAs Stripping Phenomena in galaxies with MUSE (GASP[2]), an ESO Large programme that exploits the integral-field spectrograph MUSE mounted at the VLT with the aim to characterize where, how and why gas can get removed from galaxies in different environments. A complete description of the survey strategy, data reduction and analysis procedures are presented in Poggianti et al. (2017, Paper I).

Section 2 presents the data sample and the data analysis, while Section 3 includes the results. We study the spatially resolved SFR–M_* relation (Σ_{SFR}–Σ_*) for all galaxies (Section 3.1) and also for each galaxy separately (Section 3.2), emphasizing the galaxy-by-galaxy variations. We show how the variation is mainly due to the presence of bright off-centre Hα knots, whose spatial distribution is different from one object to the other and whose Σ_{SFR} is not strictly related to the value of Σ_* in the same resolution element. We also investigate the relationship between Σ_{SFR} and total gas surface density ($\Sigma_{tot\,gas}$) (Section 3.3) and connect the local and global relations (Section 3.4), showing how the latter is a by-product of the galaxy size mass relation. In Section 4 we discuss the results and conclude.

Throughout all the papers of the GASP series, we adopt a Chabrier (2003) initial mass function (IMF) in the mass range 0.1–100 M$_\odot$. The cosmological constants assumed are $\Omega_m = 0.3$, $\Omega_\Lambda = 0.7$, and $H_0 = 70$ km s^{-1} Mpc^{-1}.

2 DATA SAMPLE, OBSERVATIONS, AND DATA ANALYSIS

The GASP targets are at redshift $0.04 < z < 0.1$, span a wide range of galaxy stellar masses, from 10^9 to $10^{11.5}$ M$_\odot$ and are located in different environments (galaxy clusters, groups, filaments, and isolated). The GASP project observed 114 galaxies in total. 76 of them are in clusters and 38 of them are in the less massive environments. The sample includes both galaxies selected as stripping candidates and undisturbed galaxies. A complete description of the survey strategy, observations, data reduction, and analysis procedure is presented in Paper I.

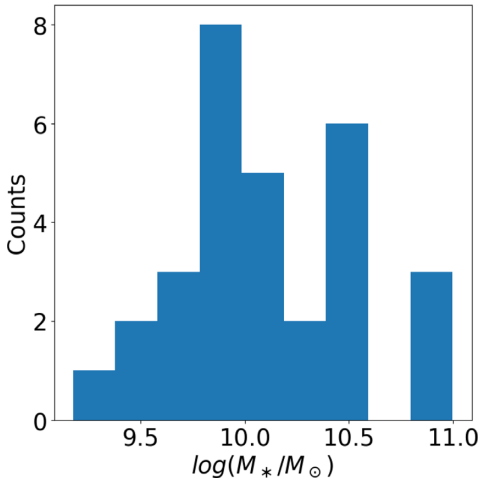

Figure 1. Total stellar mass distribution of the galaxies analysed in this work.

We stress that our observations cover the entire optical extension of the galaxy (see below for the definition of the galaxy sizes), up to several effective radii, so our data are not affected by aperture loss.

2.1 Data sample

For this work we exploit the control sample selected in Vulcani et al. (2018, Paper XIV). They extracted from the cluster + field control sample those galaxies that indeed are undisturbed and do not show any clear sign of environmental effects (ram pressure stripping, tidal interaction, mergers, gas accretion, etc.) on their spatially resolved star formation distribution, for a total of 16 cluster members and 14 field galaxies. We refer to table 2 of Paper XIV for the list of the objects, along with redshifts, coordinates, integrated stellar masses, and star formation rates. We remove from their sample JO93 and P19482 that, after a careful inspection of their Hα maps, turned out to be in an initial phase of stripping. Fig. 1 shows the total stellar mass distribution of the galaxies entering the sample, while Fig. 2 presents an overview of the sample, sorted by increasing total stellar mass, and shows the colour composite images of the targets, obtained combining the reconstructed g, r, and i filters from the MUSE datacube. As galaxies are drawn from different environments, we highlight with a red square the galaxies belonging to the cluster sample, and with a blue square those belonging to the field. This colour scheme will be adopted throughout the paper. Cluster galaxies are found at intermediate projected cluster centric distances, in the range 0.7–1.3 R_{200}.

2.2 Data analysis

As extensively presented in Paper I, we corrected the reduced datacube for extinction due to our Galaxy and subtracted the stellar-only component of each spectrum derived with our spectrophotometric code SINOPSIS (Fritz et al. 2017). In addition to the best-fitting

[2]http://web.oapd.inaf.it/gasp/index.html

Downloaded from https://academic.oup.com/mnras/article/488/2/1597/5528330 by CIS Psicologia Biblioteca F.Metelli - Universita degli Studi di Padova user on 03 November 2020

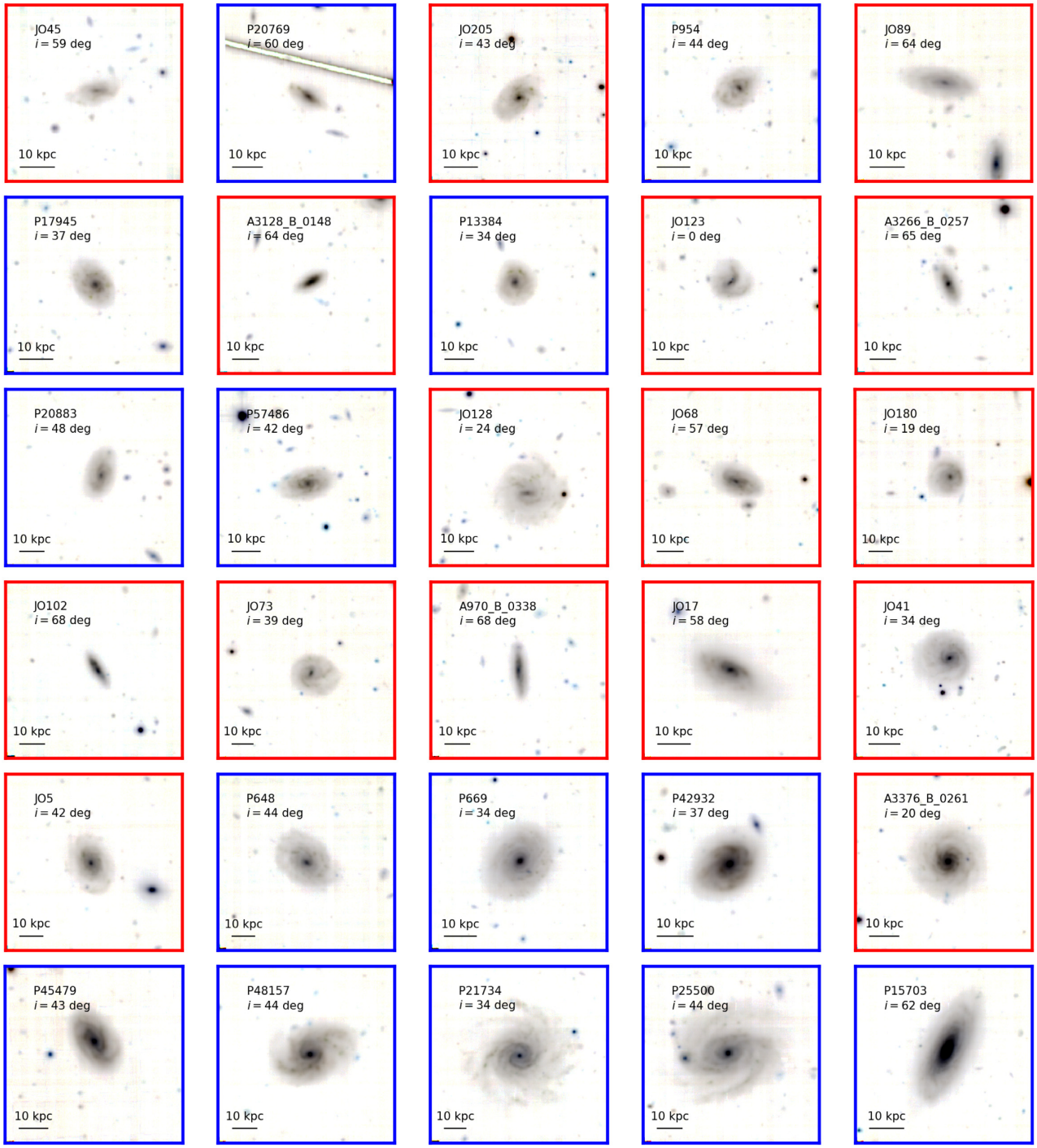

Figure 2. RGB images of the galaxies used in this paper, sorted by increasing stellar mass. The reconstructed *g*, *r*, *i* filters from the MUSE cube have been used. Colour map is inverted for display purposes. North is up, and east is left. Galaxies surrounded by a red square belong to clusters, galaxies surrounded by a blue square belong to the field. In each panel, the galaxy inclination is also given.

stellar-only model cube that is subtracted from the observed cube, SINOPSIS provides for each MUSE spaxel stellar masses, luminosity-weighted and mass-weighted ages, and star formation histories in four broad age bins.

We then derived emission line fluxes with associated errors using KUBEVIZ (Fossati et al. 2016), an IDL public software. We consider as reliable only spaxels with S/N(Hα)>5. Hα luminosities corrected both for stellar absorption and for dust extinction were used to compute SFRs, adopting the Kennicutt (1998a)'s relation: $\mathrm{SFR}(\mathrm{M}_\odot\,\mathrm{yr}^{-1}) = 4.6 \times 10^{-42} \mathrm{L}_{\mathrm{H}\alpha}(\mathrm{erg\,s}^{-2})$. The extinction is estimated from the Balmer decrement assuming a value $\mathrm{H}\alpha/\mathrm{H}\beta = 2.86$ and the Cardelli, Clayton & Mathis (1989) extinction law. The MUSE data reach a surface brightness detection limit of $V \sim 27\,\mathrm{mag\,arcsec}^{-2}$ and $\mathrm{H}\alpha \sim 10^{-17.6}\,\mathrm{erg\,s}^{-1}\,\mathrm{cm}^{-2}\,\mathrm{arcsec}^{-2}$ at the 3σ confidence level (Paper I), which translate into a Σ_{SFR} limit of $\sim 7 \times 10^{-5}\,\mathrm{M}_\odot\,\mathrm{yr}^{-1}\,\mathrm{kpc}^{-2}$.

Downloaded from https://academic.oup.com/mnras/article/488/2/1597/5528330 by CIS Psicologia Biblioteca F.Metelli - Universita degli Studi di Padova user on 03 November 2020

We used the extinction also to derive the gas mass density, using the empirical relation discussed in Barrera-Ballesteros et al. (2018): $\Sigma_{\rm tot\,gas} = 30 \times (A_{\rm v}/{\rm mag})$ ($M_\odot\,{\rm pc}^{-2}$). This relationship was calibrated using the observed gas mass density from spatially resolved observations of CO and the *V*-band attenuation for galaxies in the CALIFA EDGE survey (Bolatto et al. 2017).

We employed the standard diagnostic diagram [O III]5007/Hβ versus [O I]6300/Hα to separate the regions powered by star formation from regions powered by AGN or LINER emission. Only spaxels with an S/N > 3 in all emission lines involved are considered. We adopted the division lines by Kauffmann et al. (2003b). For the majority of the galaxies most of the Hα is powered by photoionization (plots not shown), and no galaxy in the sample hosts an AGN in its centre. To compute SFRs, we considered only the spaxels whose ionized flux is powered by star formation.

As largely discussed by Poggianti et al. (2019, Paper XIII), the diagnostic diagram based on the [O I] is generally very sensitive to physical processes different from star formation, such as thermal conduction from the surrounding hot ICM, turbulence, and shocks. Our choice to use the [O I]-based diagnostic diagram instead of other available line-ratio diagrams can therefore be considered as a conservative lower limit of the real star formation budget. Appendix A will discuss some results using the [N II]-based diagnostic diagram, for comparison.

For each spaxel in each galaxy we also computed the galactocentric radius fixing the centre of the galaxy to the peak of the stellar mass map. The radius is then expressed in units of $r_{\rm e}$, which is computed on *I*-band images by measuring the radius of an ellipse including half of the total light of the galaxy (Vulcani et al. 2019 – Paper XVI; Franchetto et al., in preparation). We remind the reader that our observational strategy allows us to detect Hα also in the galaxy outskirts: 75 per cent of the sample have a Hα coverage larger than $2.7r_{\rm e}$. This maximum extension of the Hα disc in units of $r_{\rm e}$ is independent of stellar mass (plot not shown).

We correct all quantities for the effect of inclination. We note however that no edge-on galaxy is present in the sample: galaxies span the range $20^\circ < i < 70^\circ$.

3 RESULTS

3.1 The $\Sigma_{\rm SFR}$–Σ_* relation of all galaxies

The total integrated SFR–M_* relation for the sample has been presented in Paper XIV,[3] here we focus on the spatially resolved relation.

The upper left panel of Fig. 3 shows the $\Sigma_{\rm SFR}$–Σ_* relation, using all the 92 020 star-forming spaxels included in our sample. The effective threshold in spatially resolved specific SFR entailed by the adopted cuts in S/N corresponds to $10^{-11.2}\,{\rm yr}^{-1}\,{\rm kpc}^{-2}$ and it is also shown. By selection, 99 per cent of the spaxels stay above the threshold. A correlation between the two quantities is immediately visible, with more massive spaxels typically having higher values of SFR, even though the scatter of the relation is quite large. To compute the scatter, we subdivided the sample in 10 Σ_* bins and computed the standard deviation of $\Sigma_{\rm SFR}$ in each bin separately. We then took the mean value as typical scatter, which turns out to be ∼0.3 dex. The correlation spans almost five orders of magnitude in Σ_* and three in $\Sigma_{\rm SFR}$.

We compare our results with those presented in Cano-Díaz et al. (2016) and Hsieh et al. (2017). Both studies have highlighted that the $\Sigma_{\rm SFR}$–Σ_* relation is rather tight, having a standard deviation of at most 0.2 dex, and has a slope of ∼0.7. Cano-Díaz et al. (2016) based their analysis on CALIFA data, and analysed 306 galaxies of all morphological types and environments, with inclinations <60°, in the redshift range $0.005 < z < 0.03$ and in the mass range $10^{9.7} < M_\odot < 10^{11.4}$. The CALIFA observational strategy guarantees a coverage of the spatial extension of the galaxies up to 2.5 effective radii, and spatial resolution of ∼1 kpc at the average redshift of the survey. To select regions powered by star formation, they used both the BPT diagrams based on [N II] and the WHAN diagram (Cid Fernandes et al. 2011) [EW(Hα) > 6].

The analysis by Hsieh et al. (2017) is based on MaNGA data. Their targets were selected to represent the overall galaxy population with stellar masses greater than $10^9\,M_\odot$ at $0.01 < z < 0.15$. 1085 non-interacting galaxies entered their selection. The MaNGA observational strategy guarantees a coverage of the spatial extension of the galaxies up to 1.5–2.5 effective radii, and spatial resolution of ∼1 kpc at the average redshift of the survey. To select regions powered by star formation, they used both the BPT diagrams based on [S II] and a modified version of the WHAN diagram (Cid Fernandes et al. 2011) [$\log([{\rm N\,II}]/{\rm H}\alpha) < -0.4$ and EW(Hα) > 5]. To compute the fit to the relation, they applied both the ordinary least-squares method and the orthogonal distance regression.

Qualitatively, our relation, fitted with a linear least-squares regression, is much broader and steeper, having a slope of 1.56 ± 0.07. Quantitative comparisons between ours and their analyses is not possible, as works did not specify the spatial extension coverage of the galaxies that entered their samples, nor the minimum Σ_* and $\Sigma_{\rm SFR}$ reached by their galaxies. In addition, different selection criteria have been adopted to select regions photoionized by star formation. All these aspects, along with the sample selection, analysing method, fitting recipe and spatial resolution, play important roles in the determination of the slope of the fit. Overall, literature results range from 0.6 to >1 (see also Sánchez 2013; Wuyts et al. 2013; Abdurro'uf & Masayuki 2017; Hsieh et al. 2017; Maragkoudakis et al. 2017).

To mimic the effect of the different spatial coverage on galaxies and different mass ranges probed, Fig. 3 also shows the $\Sigma_{\rm SFR}$–Σ_* relation using only the spaxels within 1 and 0.6 $r_{\rm e}$, and in three different mass bins. It unveils that relations get steeper and shift to higher Σ_* values when spaxels at large galactocentric distances are excluded from the fit, as shown by the position of the fitting line in Fig. 3. This is true both for the entire population and for galaxies in a given stellar mass bin. At each given galactocentric distance, the fit also shifts to higher Σ_* values going from low to high-mass galaxies. It appears evident that relations have smaller scatter when considering only central spaxels and less massive galaxies, even though the smallest scatter is always >0.2 dex. Most of the spaxels with $\Sigma_* \leq 10^7 M_\odot\,{\rm pc}^{-2}$ are found only in the external regions. Note that this is approximately the same radial regime where Erroz-Ferrer et al. (2019) found a breakdown of the relation, above which the relation is steeper and below which it is flatter.

Galaxy outskirts – most likely missed by previous larger surveys – might be subject to different physical processes and therefore follow less tight relations, broadening the overall trends.

It is also interesting to note that in the most massive bin there are hints for the coexistence of two parallel relations: one produced by the spaxels in the regions <0.6 $r_{\rm e}$ and, shifted towards lower

[3]Note that in Paper XIV we identified regions powered by star formation using the diagnostic diagrams based on the [N II] line rather than those based on the [O I] line. However, this choice does not affect the results, therefore we do not discuss again the global SFR–M_* relation of the sample.

Downloaded from https://academic.oup.com/mnras/article/488/2/1597/5528330 by CIS Psicologia Biblioteca F.Metelli - Universita degli Studi di Padova user on 03 November 2020

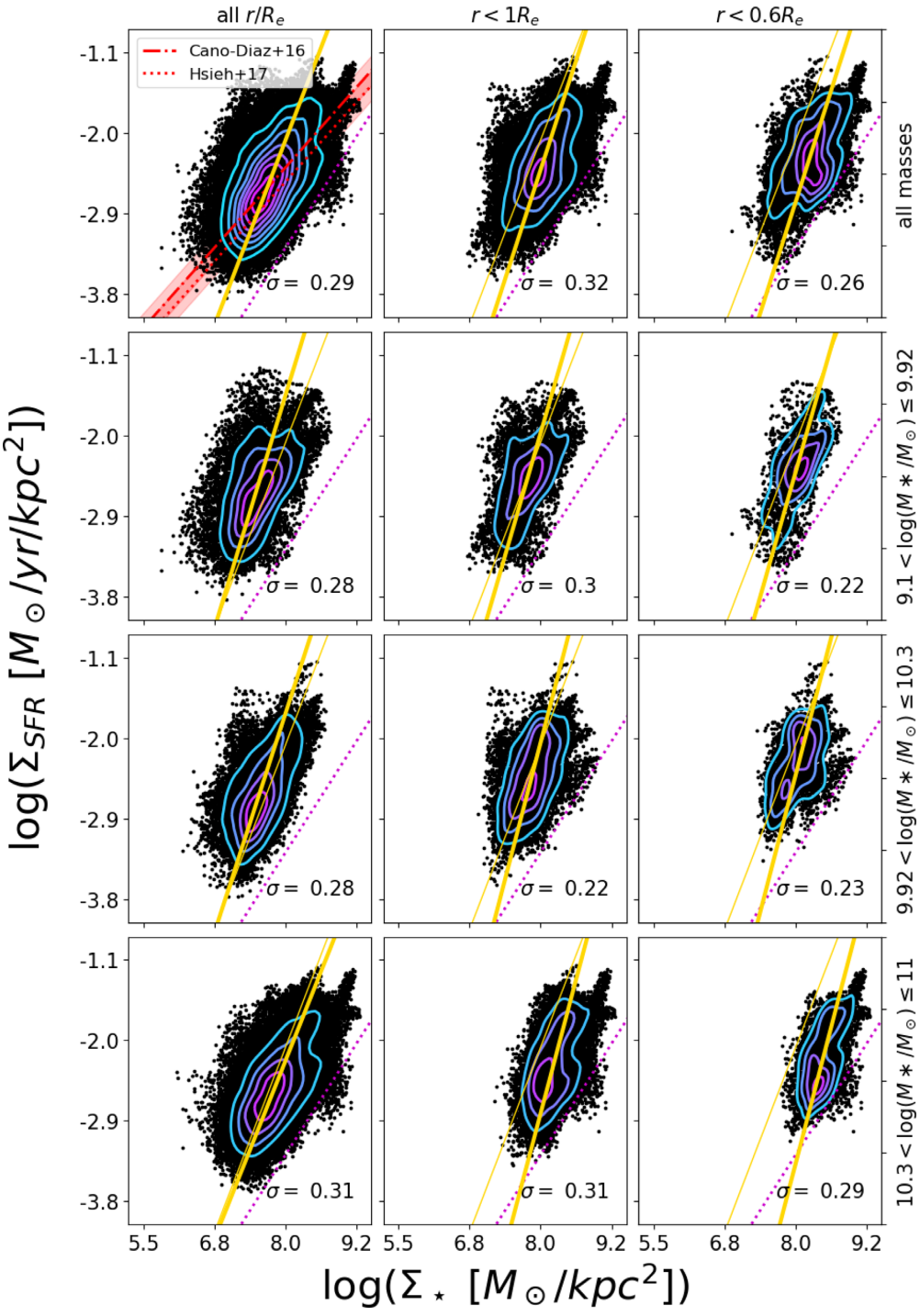

Figure 3. Spatially resolved SFR–M_* relation using all spaxels of all galaxies in the sample (left), the spaxels within $1r_e$ (central) and the spaxels within $0.6r_e$ (right), both for all galaxies together (upper row) and for galaxies in three different mass bins, as indicated in the left labels. Thick gold lines show the fit to the relation, the thin gold line shows the fit obtained in the first panel, for comparison. In the first panel, results from Cano-Díaz et al. (2016) and Hsieh et al. (2017) are reported in red, for comparison, after converted to the same IMF. Contours identify regions characterized of similar density of points. The magenta dotted line represents the effective threshold in spatially resolved specific SFR entailed by the adopted cuts in S/N corresponds to $10^{-11.2}$ yr^{-1} kpc^{-2}.

Σ_* values, one produced by the spaxels in the intermediate regions ($0.6 < r/r_e < 1$). This behaviour is not visible at lower masses. The highest mass bin includes galaxies more massive than 3×10^{10} $M_\odot$, which is a well-known discriminating value in galaxy evolution. Kauffmann et al. (2003a) were the first to show that galaxies less massive than this value have low surface mass densities, low-concentration indices typical of discs and young stellar populations. More massive galaxies have high surface mass densities, high-concentration indices typical of bulges, and predominantly old stellar populations.

We note that, plotting at the same time all galaxies together, it is not clear whether they all follow similar relations or if each galaxy

Downloaded from https://academic.oup.com/mnras/article/488/2/1597/5528330 by CIS Psicologia Biblioteca F.Metelli - Universita degli Studi di Padova user on 03 November 2020

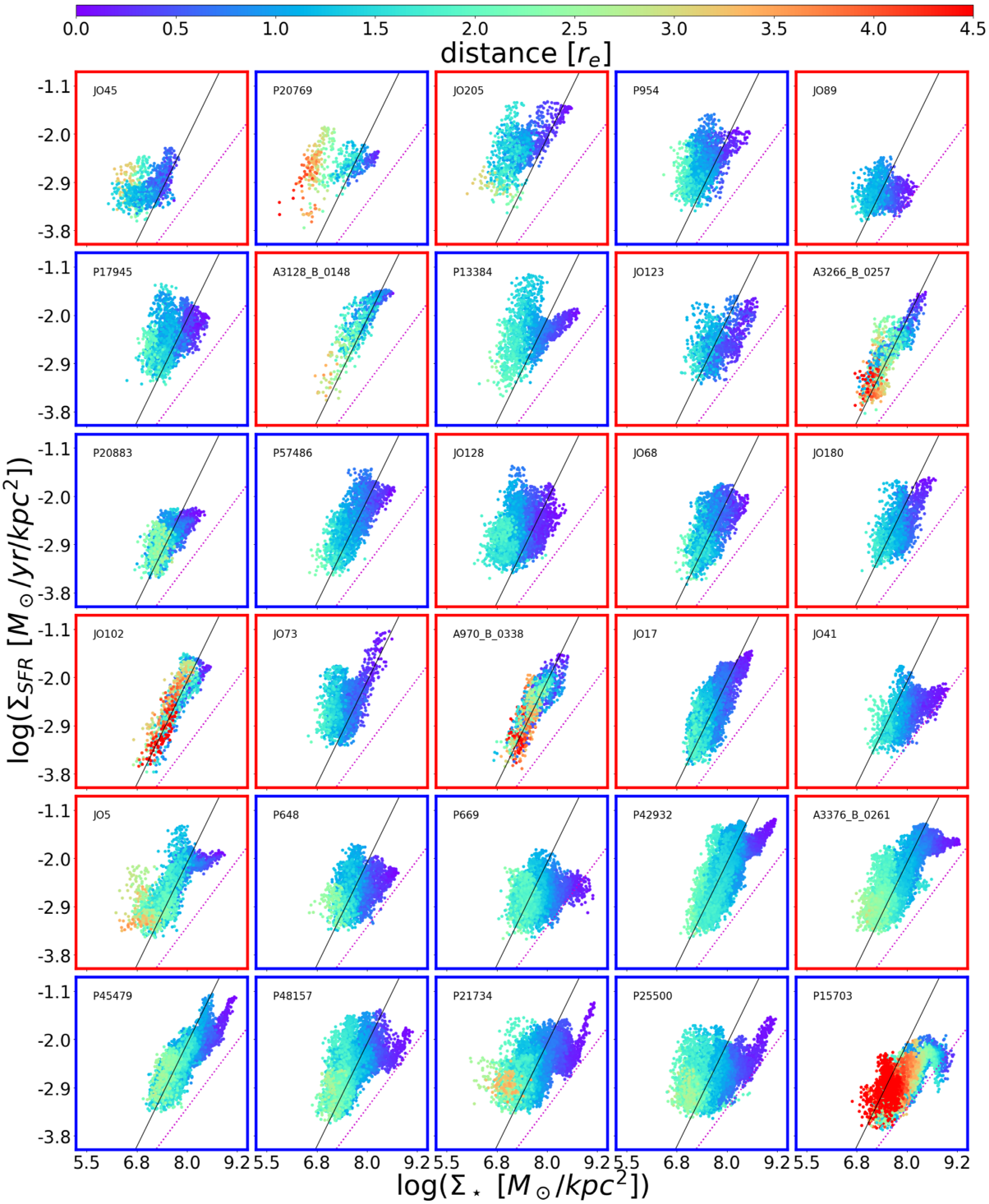

Figure 4. Σ_{SFR}–Σ_* relation for all galaxies in the sample, sorted by increasing stellar mass and colour coded by the galactocentric distance of each spaxel, in unit of r_e. Galaxies surrounded by a red square belong to clusters, galaxies surrounded by a blue square belong to the field. The black line represents the fit to the whole sample, from Fig. 3. The magenta dotted line represents the effective threshold in spatially resolved specific SFR entailed by the adopted cuts in S/N corresponds to $10^{-11.2}$ yr^{-1} kpc^{-2}.

is characterized by a different slope, intercept, scatter. In the next subsection we therefore characterize each galaxy separately.

3.2 The galaxy-by-galaxy Σ_{SFR}–Σ_* relation

Fig. 4 presents the Σ_{SFR}–Σ_* relation for each galaxy separately, distinguishing among spaxels at different galactocentric distances. It appears evident that, even though overall in most cases a correlation does exist, each object spans a distinct locus on the Σ_{SFR}–Σ_* plane (in agreement with Hall et al. 2018) and the relation that better describes it is characterized by a different slope and scatter. Table 1 presents the slope, intercept, coefficient correlation value (r_value), the scatter, and the standard error of the estimate for each galaxy separately. Half of the sample has r_value < 0.5, indicating there is

Downloaded from https://academic.oup.com/mnras/article/488/2/1597/5528330 by CIS Psicologia Biblioteca F.Metelli - Universita degli Studi di Padova user on 03 November 2020

Table 1. Least-squares regression parameters for each galaxy.

ID	Slope	Intercept	r_value	std_err	Scatter
A3128_B_0148	1.01	− 10.04	0.866	0.024	0.24
JO102	1.2	− 11.67	0.852	0.025	0.27
A3266_B_0257	1.05	− 10.6	0.833	0.023	0.28
P45479	0.8	− 8.65	0.82	0.008	0.19
A3376_B_0261	0.84	− 8.91	0.817	0.007	0.24
A970_B_0338	1.06	− 10.62	0.815	0.023	0.23
P15703	0.63	− 7.72	0.765	0.007	0.22
JO5	0.76	− 8.25	0.763	0.012	0.21
JO17	1.08	− 10.9	0.761	0.015	0.25
P42932	0.91	− 9.47	0.745	0.009	0.23
P57486	0.88	− 9.18	0.718	0.018	0.2
P20883	0.62	− 7.43	0.653	0.016	0.22
JO205	0.56	− 6.37	0.626	0.021	0.23
JO68	0.8	− 8.67	0.617	0.023	0.29
P21734	0.48	− 6.21	0.605	0.007	0.22
P48157	0.61	− 7.12	0.595	0.01	0.26
JO180	0.66	− 7.7	0.533	0.026	0.16
JO41	0.44	− 6.13	0.525	0.016	0.21
JO123	0.47	− 6.18	0.502	0.024	0.22
JO73	0.57	− 6.77	0.471	0.024	0.33
P954	0.51	− 6.33	0.466	0.022	0.28
JO45	0.33	− 5.25	0.442	0.022	0.17
P17945	0.45	− 5.82	0.435	0.019	0.28
P25500	0.3	− 4.94	0.41	0.007	0.27
P13384	0.34	− 4.93	0.378	0.021	0.25
P648	0.33	− 5.11	0.347	0.015	0.19
JO128	0.34	− 5.12	0.343	0.014	0.28
P20769	0.18	− 3.9	0.323	0.024	0.21
P669	0.15	− 3.83	0.22	0.009	0.23
JO89	0.07	− 3.57	0.09	0.022	0.19

no correlation between the Σ_{SFR} and Σ_* and suggesting that fitting relations is meaningless. Only 6/30 galaxies have r_value > 0.8, suggesting a rather strong correlation. In all cases the *p*-value is close to zero, supporting the reliability of the results.

The slope of the relation for each of the individual galaxies is close to one, especially for those with the highest r_value, and even shallower when the correlation is weaker. The steep slope of the global relation (Fig. 3) is therefore probably a consequence of the different intercepts of the galaxies in the sample.

We note that masking the spaxels most likely located in the galaxy bulge – whose size has been obtained applying a 2D fitting on the *i*-band images (see Franchetto et al., in preparation) – does not affect the results. We therefore include them in the forthcoming analysis.

Some galaxies show quite elongated sequences (e.g. A3128_B_0148, P57486), while in some other cases a cloud rather than a sequence is observed (e.g. JO45, JO89). Few galaxies really show a flattening (A3376_B_0261, P669) or bending (P48157, P15703) of the relation at higher Σ_* values. Note that this behaviour is not due to the presence of the bulge, as trends stay also when the contribution of the bulge is removed (plot not shown). Moretti et al. (in preparation) will provide a detailed description of these objects presenting anomalies in the central regions.

For some galaxies the scatter increases with decreasing Σ_* (e.g. P25500), for some others different sequences coexist (e.g. P20769, P13384, JO5). Only a few galaxies show a really tight and unique sequence (e.g. A3128_B_0148, JO102, A970_B_0338). The latter are all in clusters. Apart from that, no other outstanding environmental effects are evident. This result is somehow expected, given that the cluster members in the control sample most likely just entered the cluster environment from the field and have had not time yet to feel cluster specific processes. This is confirmed by the location in projected phase space (plot not shown): their cluster centric distribution spans from 0.7 to 1.3 R_{200}, and their relative velocities are within $|\Delta(v)|/\sigma_{cl}<2$, where $\Delta(v)$ is the galaxy velocity with respect to the velocity of the cluster and σ_{cl} is the velocity dispersion of the cluster, consistent with the fact that they have not approached yet the cluster centre.

To better highlight the galaxy-by-galaxy variations with respect to the relation obtained considering all galaxies together, for each galaxy we compute the difference between the galaxy Σ_{SFR} and their expected value according to the fit to the entire sample (Fig. 3), given their Σ_*. Fig. 5 shows the distribution of these differences for each galaxy separately. If a galaxy had the same Σ_{SFR}–Σ_* as the entire sample, the median value of the distribution would be 0 (marked by a black line in the plot). In each panel, the cyan line shows the median of the distribution and in many cases it coincides with the black line (e.g. JO17, JO68, A3376_B_0261). In contrast, for some galaxies (e.g. JO45, JO41, JO205, P15703), the median of the distribution is significantly different, suggesting that the Σ_{SFR}–Σ_* of the galaxy significantly deviates from the total one. In addition to the median values, also the shapes of the distributions give important information: while in some cases they are quite narrow (e.g. A970_B_0338, A3128_B_0148), in many other cases they are broad (e.g. P13384), show asymmetric tails (e.g. JO45), and are even double peaked (e.g. P20769). These results highlight that no a universal Σ_{SFR}–Σ_* relation exists for the galaxies.

Fig. 4 also allows to inspect the position of each spaxel with respect to the galaxy centre. Considering galactocentric distance, we find that spaxels in the external regions are characterized by systematic lower Σ_* values, and spaxels at similar distance in terms of r_e are distributed in the Σ_{SFR}–Σ_* plot on almost vertical relations, suggesting that the correlation between Σ_{SFR} and distance might be stronger than Σ_{SFR} and Σ_*. None the less, if we contrast the Σ_{SFR} and distance, we find relations as broad as those presented in Fig. 4, having a similar scatter (plot not shown).

To better characterize the galaxy-by-galaxy variations, we consider separately the spaxels in three equally spaced mass density bins, centred at $\Sigma_* \sim 6.3 \times 10^6$, $\sim 6.3 \times 10^7$, $\sim 6.3 \times 10^8$ $M_\odot$ kpc^{-2}, and compute the median Σ_{SFR} along with the scatter, measured as one standard deviation. The left-hand panel of Fig. 6 shows these values for each galaxy separately, sorted by increasing total stellar mass. The scatter ranges from 0.2 to 0.3 dex in the three bins. Even though almost all the plotted points agree within the errors with the median values, this figure shows again that each galaxy is characterized by a different slope and scatter in the Σ_{SFR}–Σ_* relation. In addition, it appears evident that while at intermediate values of Σ_* galaxies have Σ_{SFR} values similar to what expected from the total fit, both at low and high Σ_* values they strongly deviate from it, being systematically higher and lower, respectively.

The right-hand panel of Fig. 6 shows the median Σ_{SFR} along with the scatter of the spaxels in four different galactocentric distance bins. The galaxy by galaxy variation is outstanding, especially for $r/r_e < 1$, suggesting that regions characterized by high values of star formation can be present at different distances in different galaxies. The scatter is always large, ranging from 0.15 to 0.35 dex. In the next section we will focus on these off-centre star-forming regions.

Taken together, Figs 4 and 6 indicate that variations are evident not only among different galaxies, but also among regions within galaxies (defined according to galactocentric distance,

Downloaded from https://academic.oup.com/mnras/article/488/2/1597/5528330 by CIS Psicologia Biblioteca F.Metelli - Universita degli Studi di Padova user on 03 November 2020

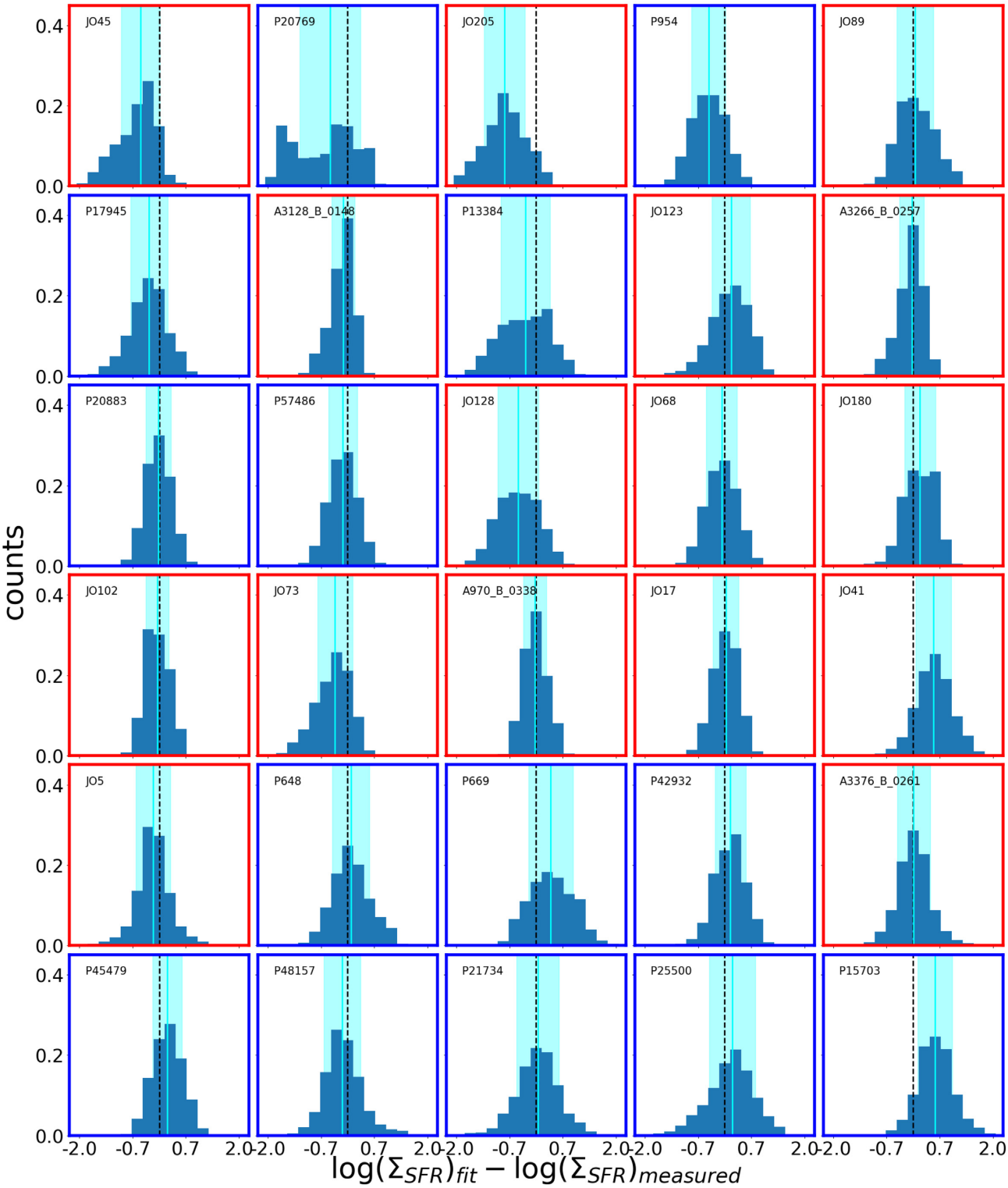

Figure 5. For each galaxy, distribution of the differences between the galaxy $\Sigma_{\rm SFR}$ and their expected value according to the fit to the entire sample (Fig. 3), given their Σ_*. The black line is always centred at 0, the cyan lines and shaded area give median values and the standard deviation of the distribution (1σ). Galaxies are sorted by increasing stellar mass. Galaxies surrounded by a red square belong to clusters, galaxies surrounded by a blue square belong to the field.

$\Sigma_{\rm SFR}$ or Σ_*), implying that there is no 'universal' relation between Σ_* and $\Sigma_{\rm SFR}$.

We note that we have investigated whether the magnitude of the scatter depends on a number of global parameters, namely the total stellar mass, the SFR, the Δ(SFR) – i.e. the differences between the galaxy SFRs and their expected value according to the fit of the SFR–M_* relation, given their mass (Paper XIV), the galaxy inclination, the number of knots, the SFR in the knots, the SFR in

Downloaded from https://academic.oup.com/mnras/article/488/2/1597/5528330 by CIS Psicologia Biblioteca F.Metelli - Universita degli Studi di Padova user on 03 November 2020

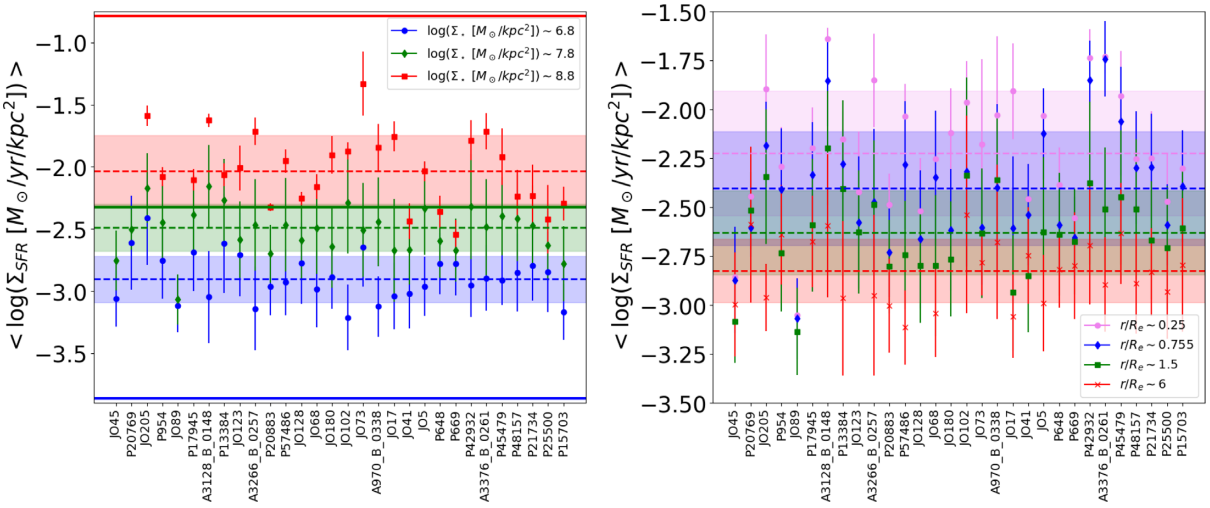

Figure 6. Median Σ_{SFR} in three Σ_* bins (left) and in four galactocentric distance bins (right), for all galaxies in the sample, sorted by increasing stellar mass. In both panels error bars represent the standard deviation. In the left-hand panel, dashed horizontal lines represent median values in each Σ_* bin, solid lines represent expected values given the fit of the total relation for that bin. In the right-hand panel, dashed horizontal lines represent median values in each bin of distance. Shaded areas are the standard deviation of the medians.

the knots divided by the total stellar mass, the effective radius, but found no statistically significant trends. Appendix B better discusses this point.

3.2.1 Star-forming knots and diffuse emission

There are several parameters that might drive the Σ_{SFR}–Σ_* relations. One of these is the presence and spatial distribution of concentrated star-forming regions, spread throughout the galaxy disc. Indeed, Fig. 7 shows that the all galaxies present bright Hα knots with Hα surface brightness typically between $10^{-16.5}$ and 10^{-15} erg s^{-1} cm^{-2} arcsec^{-2}. As discussed also in Paper I and Paper XIII, these are star-forming clumps embedded in regions of more diffuse emission. Paper I describes in detail how these clumps are identified. Briefly, a shell script including IRAF and FORTRAN routines has been developed. The script searches the local minima of the laplace + median filtered Hα MUSE image. The boundaries of these clumps (i.e. their radius, having assumed circular symmetry) are estimated considering outgoing shells until the average counts reach a threshold value that defines the underlying diffuse emission.

Both the number of knots and the total SFR in these knots are somehow correlated with the total mass of the galaxy, even though a quite spread exist, as shown in Fig. 8 (see also Paper XIII). The more massive the galaxy the higher the number of knots. The right-hand panel of the figure shows that the SFR in the knots is systematically higher than the SFR in the diffuse component, on average by a factor of ∼7.

Fig. 9 shows the Hα luminosity of the knots as a function of the galactocentric distance in units of r_e, for each galaxy separately. Even though an overall anticorrelation exists, with more distant knots being less Hα luminous (and therefore less star forming), the relation spans over three orders of magnitude at a fixed galactocentric distance, showing how knots at the same galactocentric distance can have systematically different star-forming properties.

Fig. 10 shows the same relation shown in Fig. 4, but using different colour scales for spaxels in the knots and in the diffuse component: spaxels belonging to the bright knots are plotted using a red-yellow colour scale, spaxels belonging to the diffuse component are plotted using a blue-green colour scale. In total, 69 861 of the spaxels belong to the knots, the remaining 22 159 spaxels to the diffuse component. It is immediately clear that the Σ_{SFR}–Σ_* relations for spaxels within the knots are very broad: at any given Σ_* a large range of Σ_{SFR} values can exist. In addition, there is not always a tight correlation between galactocentric distance, Σ_* and Σ_{SFR} in the knots: highly star-forming knots are not only present in the centre of the galaxies and they not always take place in the highest surface mass density regions. The multisequences visible in the plots are due to highly star-forming knots distributed at different galactocentric distances, even at low surface mass densities. Note that if we reduced the size of the knots by half, to overcome the issue of their external regions being influenced by the diffuse component due to the size of the PSF, we obtain the same result.

In contrast, relations for the diffuse component are much tighter, though still a broadening of the relations is visible for some cases. This is even clearer in Fig. 11, where all galaxies are plotted together. It is interesting to note that, even though the scatter is much larger for spaxels in the knots than for the diffuse component, the slope and intercept of the relations are remarkably similar. We note that this result is not driven by the larger number of spaxels in the knots: we randomly extracted from the knots sample 10 subsamples with the same number of elements as the diffuse sample, finding the same result.

Fig. 12 compares the median scatter of the Σ_{SFR}–Σ_* relation obtained using the spaxels in the knots and that obtained using those in the diffuse component, highlighting how the latter is systematically lower for more than 70 per cent of the sample.

Our result suggests that bright star-forming regions follow different Σ_{SFR}–Σ_* relations from the diffuse emission.

3.3 The Σ_{SFR}–$\Sigma_{tot\,gas}$ relation

The molecular gas surface density has been found to trace the stellar mass surface density on kiloparsec scales (Lin et al. 2017). This might lead to the correlation between Σ_{SFR} and Σ_*, at a fixed SFE. Here we therefore aim at understanding whether the Σ_{SFR} correlates

Downloaded from https://academic.oup.com/mnras/article/488/2/1597/5528330 by CIS Psicologia Biblioteca F.Metelli - Universita degli Studi di Padova user on 03 November 2020

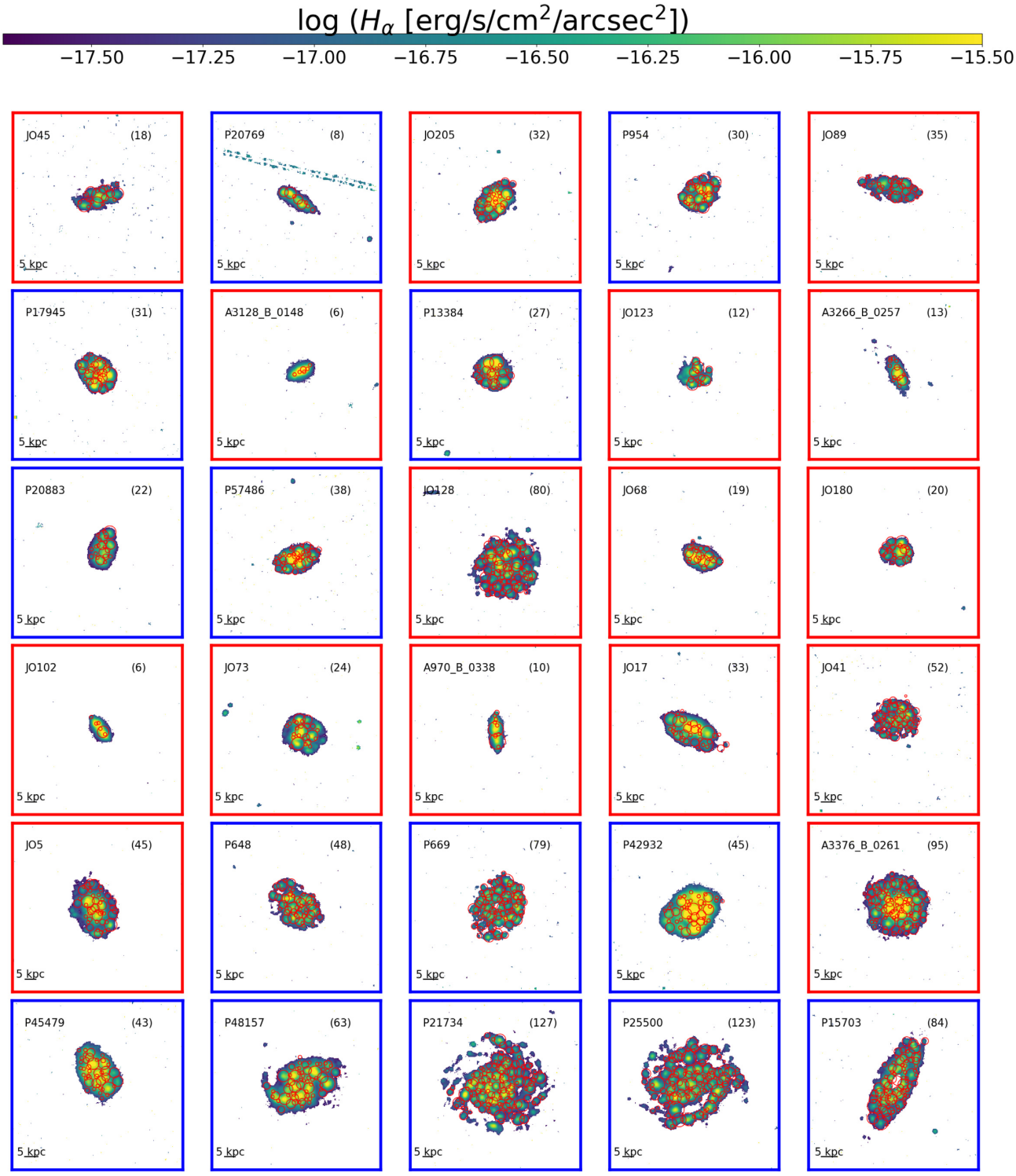

Figure 7. Hα maps for all galaxies in the sample, sorted by increasing stellar mass. Red circles show the Hα knots. Galaxies surrounded by a red square belong to clusters, and galaxies surrounded by a blue square belong to the field. Numbers in parenthesis are the number of knots in each galaxy.

better to the total gas surface density ($\Sigma_{\rm tot\,gas}$) than to the Σ_*, for both the diffuse component and the knots.

Bigiel et al. (2008) have investigated the $\Sigma_{\rm SFR}$–$\Sigma_{\rm tot\,gas}$ relationship, at sub-kpc resolution, in a sample of 18 nearby galaxies, using high-resolution H I data from The H I Nearby Galaxy Survey (THINGS, Walter et al. 2008), CO data from HERACLES (Leroy et al. 2008), and the BIMA Survey of Nearby Galaxies (SONG, Helfer et al. 2003). Their analysis was confined to the optical radius r_{25}, i.e. where the *B*-band magnitude drops below 25 mag arcsec^{-2}. Almost all star formation occurs within this radius, although they found that the H I often extends much beyond r_{25}. They found that overall the relationship has a

Downloaded from https://academic.oup.com/mnras/article/488/2/1597/5528330 by CIS Psicologia Biblioteca F.Metelli - Universita degli Studi di Padova user on 03 November 2020

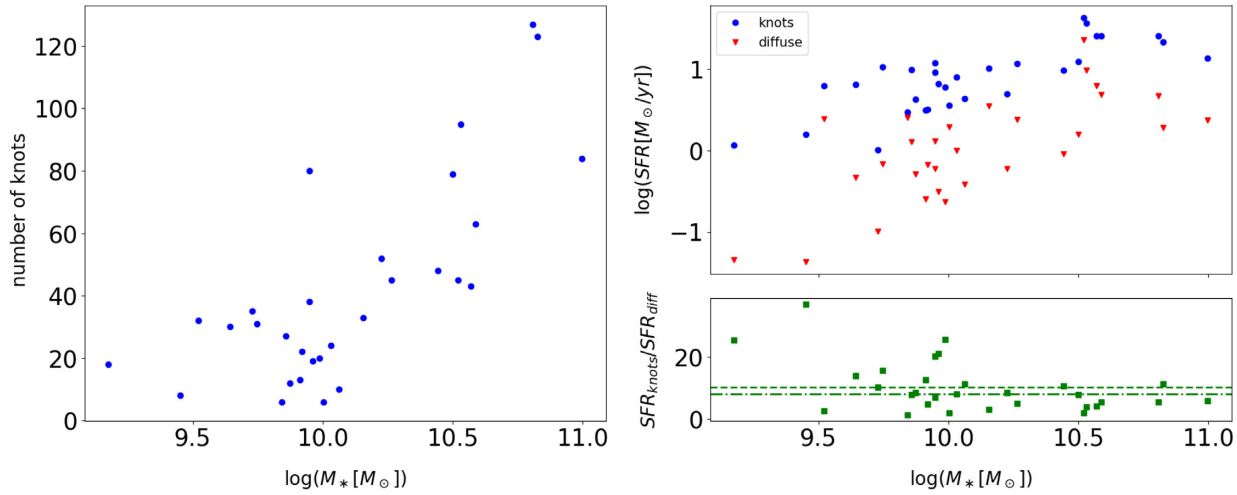

Figure 8. Number of knots (left) and SFR in the knots and in the diffuse component (right) as a function of the stellar mass, for each galaxy separately. The bottom right inset shows the ratio of the SFR between the two component, along with the median (dash–dotted) and the mean value (dashed).

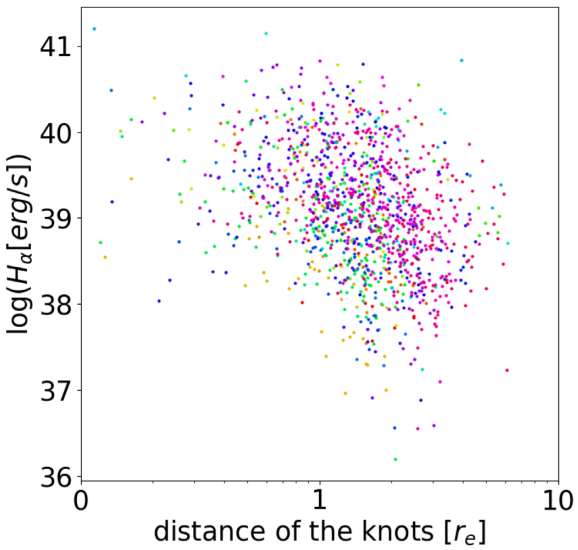

Figure 9. Hα luminosity of each knot as a function of galactocentric distance in unit of r_e, for all galaxies in the sample. Different colours refer to knots belonging to different galaxies.

scatter of ∼0.3 dex, but the distribution of points in the $\Sigma_{\rm tot\,gas}$–$\Sigma_{\rm SFR}$ parameter space varies from galaxy to galaxy, indicating that there is no universal behaviour. In some cases, a single power law relates total gas and SFR over many orders of magnitudes in gas surface density. In other cases, they found a wide range of SFRs at almost the same gas column. The two quantities seem to become essentially uncorrelated where ΣH I $>\Sigma H_2$. This transition typically occurs at $r > 0.5r_{25}$. Their analysis therefore suggests that a universal total gas Schmidt law (Kennicutt 1998b) does not exist at all galactocentric distances. According to their interpretation, galaxies with well-defined total gas Schmidt laws (and low H I surface densities) may have lost diffuse H I not associated with star formation in interactions.

Fig. 13 shows the $\Sigma_{\rm SFR}$–$\Sigma_{\rm tot\,gas}$ relationship for the GASP sample. We remind the reader that we obtained the $\Sigma_{\rm tot\,gas}$ from the A_v, using a calibration based on CO observations as we have at our disposal direct estimates of neither H I nor H_2. Note however that the A_v traces the dust heated by star formation and not the cold dust emission and Corbelli et al. (2012) have shown that the CO mass, proxy for the H_2 mass, is tightly correlated to the latter and not to the former.

Similarly to what found by Bigiel et al. (2008), we observe a large spread between the two quantities and different behaviours among the different galaxies. Typically, relations are thinner at high $\Sigma_{\rm SFR}$ values and they widen at low $\Sigma_{\rm SFR}$ values. Multisequences are observed at high $\Sigma_{\rm SFR}$ values. These ones correspond to different knots that are characterized by different Σ_* (as shown by the colour of the points) and $\Sigma_{\rm tot\,gas}$. Some galaxies lie on the Kennicutt–Schmidt law (even though with a large scatter – e.g. JO68), other lie well below it (e.g. P15703). The scatter ranges from 0.2 dex (JO89) to 0.5 dex (P42932). Considering separately the knots and the diffuse component, no significant differences are observed (plot not shown).

As Bigiel et al. (2008) found that the region at which the two quantities are essentially uncorrelated is at $r \sim 0.5r_{25}$, we investigate if also in our sample selecting only the central regions thins the relation. In our sample $r_e \sim 0.5r_{25}$ (Fasano, private communication). Considering only spaxels with $r < r_e$ (plot not shown), we obtain a scatter of ∼0.3 dex, compatible with what found by Bigiel et al. (2008). Our results therefore on one side validate the approach of using the dust extinction to compute total gas surface density, at least in the galaxy cores, and on the other side support the hypothesis that the Kennicutt–Schmidt law does not hold in the galaxy outskirts.

Finally, our results also suggest the total gas surface density is not a primary driver of the $\Sigma_{\rm SFR}$–Σ_* relation, as the $\Sigma_{\rm SFR}$–$\Sigma_{\rm tot\,gas}$ relation is not tighter than the former, when all spaxels are considered.

3.4 Spatially resolved versus global SFR–mass relation

In the previous sections we have observed that the spatially resolved SFR–M_* relation seems not to depend on the total stellar mass. Plots were sorted by increasing stellar mass but no clear trends were visible.

It is now interesting to understand how the local relation is related to the global one. Fig. 14 resembles Fig. 4, where each panel shows the $\Sigma_{\rm SFR}$–Σ_* relation for each galaxy separately. Single spaxels are represented with orange colours. Each panel also shows the

Downloaded from https://academic.oup.com/mnras/article/488/2/1597/5528330 by CIS Psicologia Biblioteca F.Metelli - Universita degli Studi di Padova user on 03 November 2020

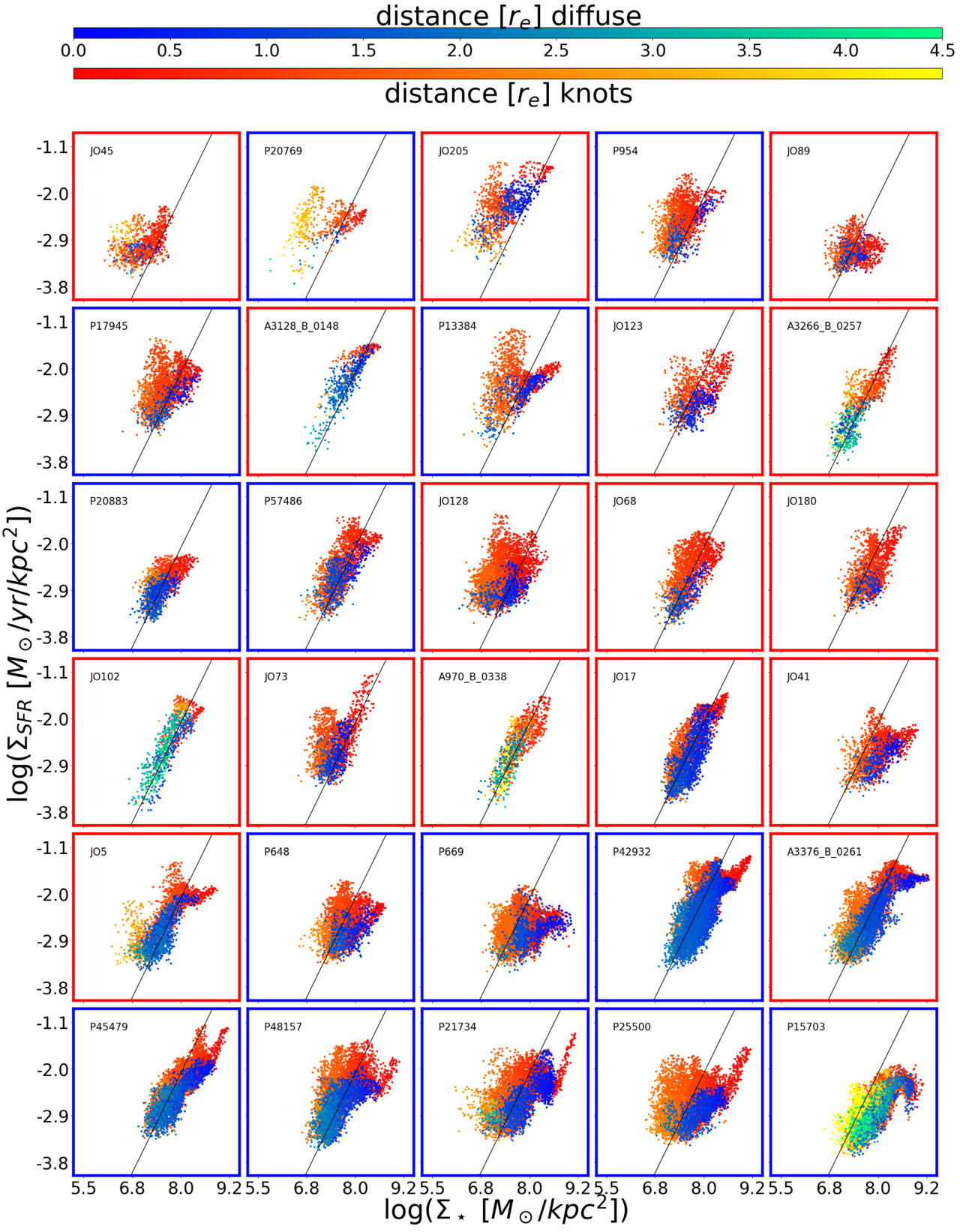

Figure 10. Σ_{SFR}–Σ_* relation for all galaxies in the sample, sorted by increasing stellar mass and colour coded by the distance, in unit of r_e. The diffuse component of the galaxies (removing the Hα knots) is plotted using a blue-green colour-scale, the knots are plotted using a red-yellow colour-scale. Galaxies surrounded by a red square belong to clusters, galaxies surrounded by a blue square belong to the field. The black line represents the fit to the whole sample, from Fig. 3.

Downloaded from https://academic.oup.com/mnras/article/488/2/1597/5528330 by CIS Psicologia Biblioteca F.Metelli - Universita degli Studi di Padova user on 03 November 2020

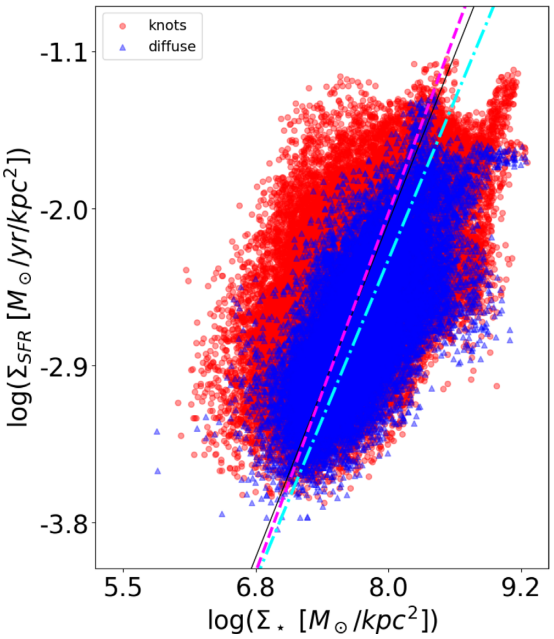

Figure 11. Σ_{SFR}–Σ_* relation for spaxels belonging to knots (red) and to the diffuse component for all galaxies in the sample together. The black line represents the fit to the whole sample, from Fig. 3, the dashed magenta line is the fit to the knots, the dash–dotted cyan line is the fit to the diffuse component.

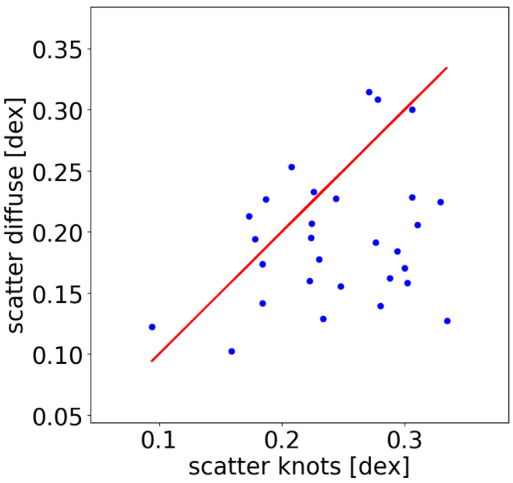

Figure 12. For each galaxy, comparison between the median scatter of the Σ_{SFR}–Σ_* relation obtained using the spaxels in the knots and that obtained using those in the diffuse component. The red line represents the 1:1 relation.

mean Σ_{SFR} and Σ_* value for each galaxy of the sample, represented by coloured circles. The circles are colour coded by the number of spaxels for which the stellar mass has been computed, used as a proxy of the galaxy size, in the corresponding galaxy. The circle surrounded by an empty magenta one indicates the values of the galaxy shown in that panel. Each panel also shows the global SFR–M_* relation of each galaxy, obtained by summing the values of all the spaxels of a given galaxy. The relation is shown with diamond symbols. As for the mean Σ_{SFR}–Σ_* relation, symbols are colour coded by the number of spaxels in that galaxy and the empty magenta diamond shows the galaxy discussed in that panel.

Fig. 14 shows that overall, the mean Σ_{SFR} and Σ_* values occupy a well defined and quite restricted region in the plane. 90 per cent of the points have Σ_{SFR} values spanning the range $(6.2-1.2) \times 10^{-2} M_\odot\ yr^{-1}\ kpc^{-2}$ and Σ_* values spanning the range $(1.6-8.2) \times 10^7\ M_\odot\ kpc^{-2}$. They therefore span a range of $\sim$0.7 dex both in surface mass density and in surface SFR density. Hence even though each galaxy is characterized by a different and overall quite spread Σ_{SFR}–Σ_* relation, average values are similar. No trends are seen for the mean Σ_{SFR} and Σ_* values with increasing number of spaxels within the galaxies, indicating that these quantities are independent on the galaxy size. In contrast, a clear trend with galaxy size is seen when global values are considered: bigger galaxies (indicated by lighter colours) are found in the upper left region of the global SFR–M_* relation, while smaller galaxies (indicated by darker colours) are preferentially located in the bottom left region. In addition, the ranges spanned by global values are almost twice as broad as those spanned by local values: SFR values range from 0.12 to 5 $M_\odot\ yr^{-1}$, stellar mass values from 8×10^8 to $5 \times 10^{10}\ M_\odot$. The relation is therefore stretched and presents a flatter fit than the fit of the local relation. This finding indicates that the global SFR–mass relation arises simply from the combination of two factors: (a) the mean spatially resolved Σ_{SFR} versus Σ_* value does not vary much for most galaxies, and (b) more massive galaxies are on average bigger (the mass–size relation), i.e. have more spaxels that contribute both to the total mass and total SFR. This stretches the relation between the two quantities into a linear and quite tight global SFR–mass relation. Thus, the global SFR–mass relation is a consequence of the mass–size relation.

4 DISCUSSION AND SUMMARY

In this paper we have reported the analysis of the spatially resolved SFR–M_* relation, based on 92 020 star-forming spaxels of 30 local undisturbed late-type galaxies in different environments drawn from the GAs stripping phenomena in galaxies with MUSE (GASP, Paper I).

The GASP survey exploits the exquisite performances of the integral-field spectrograph MUSE mounted at the VLT and one of its added values is that the observations cover the entire optical extension of the galaxy, so that we can characterize the star-forming properties up to several effective radii. Specifically, we detected Hα out of more than $2.7 r_e$ for 75 per cent of the sample analysed in this work.

Given the MUSE capabilities and observational conditions, we could recover the spatially resolved SFR–M_* relation on the kpc scale, so we are in the regime where SFR and M_* estimates are reliable. Indeed, while reaching sufficiently small spatial scales is critical to shed light on the physical processes that regulate galaxy formation, it is important to stress that measurements for the SFMS may be appropriate only on scales larger than individual giant molecular clouds (GMCs), typically of the order of 100 pc. On smaller scales, young clusters might drift from their parent GMC, thus disconnecting measurements of Σ_{SFR} from their related Σ_{gas}, therefore yielding incorrect M_* and SFR.

Star formation activity can also vary from cloud to cloud, and since most SFR transformations are generalized to be applied across all environments, sampling of statistically robust and extended star formation activity is therefore required. The smallest region size that will contain both a complete sampling of star-forming environments, IMFs used, and is not affected by the possible drift of young stellar clusters from their parent GMC is 500 pc (Kruijssen & Longmore 2014). This spatial scale must be used as the minimum

Downloaded from https://academic.oup.com/mnras/article/488/2/1597/5528330 by CIS Psicologia Biblioteca F.Metelli - Universita degli Studi di Padova user on 03 November 2020

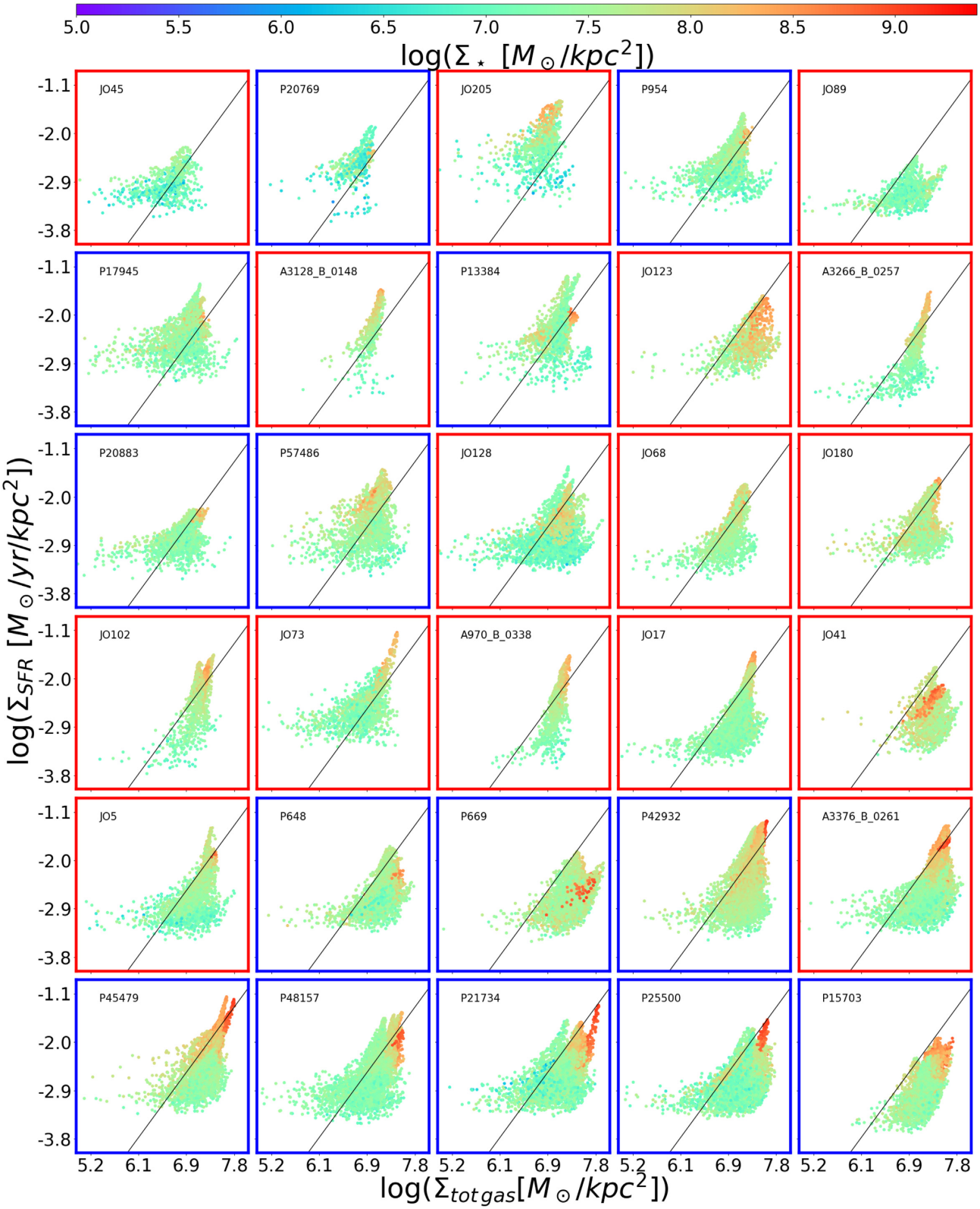

Figure 13. Spatially resolved SFR–total gas mass relation for the knots and the diffuse component together for all galaxies in the sample, sorted by total stellar mass and colour coded by the Σ_*. Black line represents the Kennicutt–Schmidt law Kennicutt (1998b). Galaxies surrounded by a red square belong to clusters, galaxies surrounded by a blue square belong to the field.

Downloaded from https://academic.oup.com/mnras/article/488/2/1597/5528330 by CIS Psicologia Biblioteca F.Metelli - Universita degli Studi di Padova user on 03 November 2020

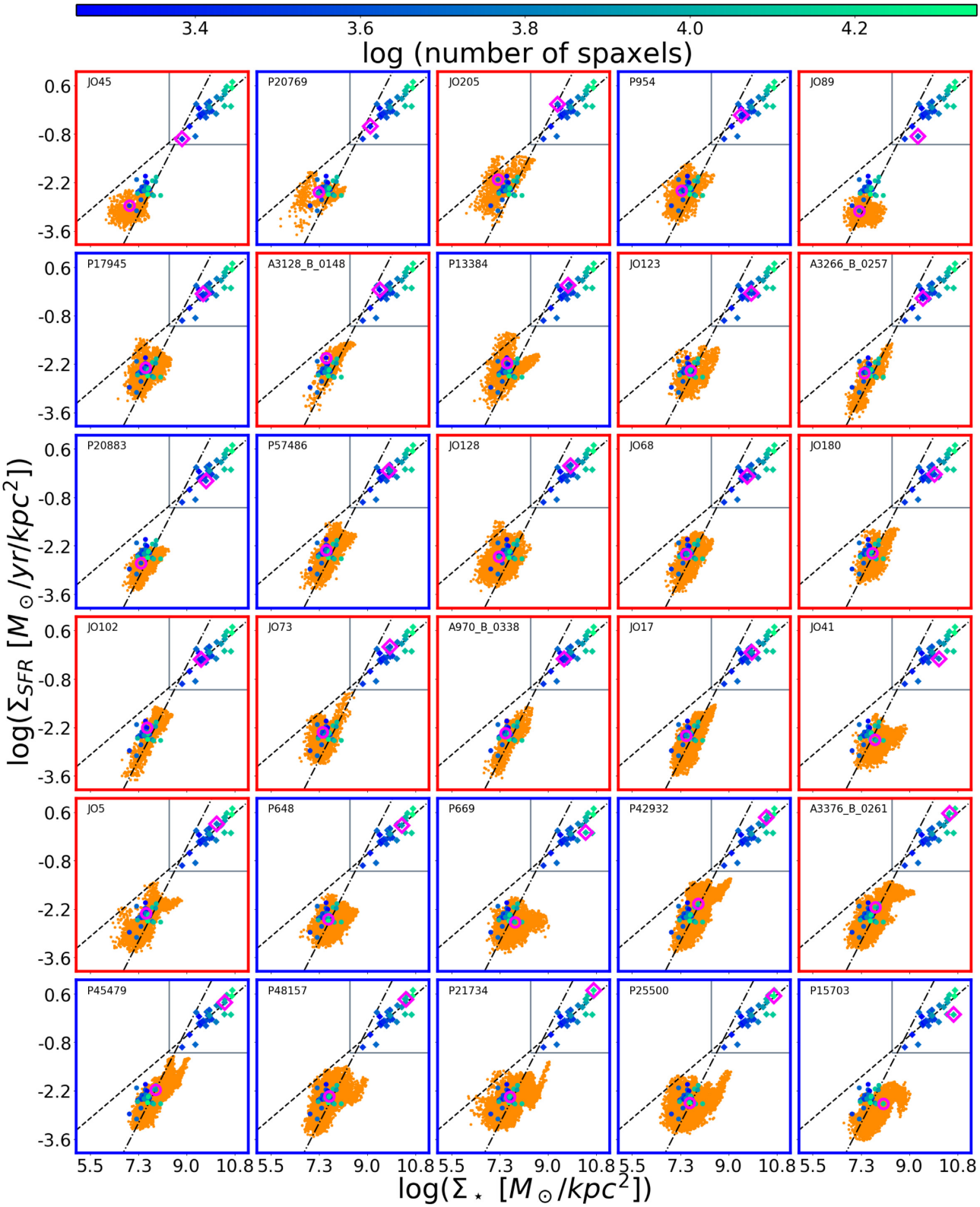

Figure 14. Comparison between the local and the global SFR–M_* relations. In each panel, the Σ_{SFR}–Σ_* relation of the galaxy listed in the upper corner is shown with orange dots. The mean Σ_{SFR} and Σ_* values of the same galaxy is shown with an empty magenta circle. Filled circles show the mean Σ_{SFR} and Σ_* values for all the galaxies. They are colour coded by the number of spaxels in each galaxy and are all the same in all the panels. The axis aligned sub-panels show the global relation, obtained by summing the values of all the spaxels in each galaxy. The x-axis shows the log (M_*[M$_\odot$]), the y-axis shows the log(SFR[M$_\odot$ yr^{-1}]). Filled diamonds are colour coded by the number of spaxels in each galaxy, the empty magenta diamond indicates the position of the galaxy shown in that panel. In all the panels, the dash–dotted line shows the fit from the upper left panel of Fig. 3, the dashed line shows the fit to the global SFR–mass relation. Galaxies surrounded by a red square belong to clusters, galaxies surrounded by a blue square belong to the field.

Downloaded from https://academic.oup.com/mnras/article/488/2/1597/5528330 by CIS Psicologia Biblioteca F.Metelli - Universita degli Studi di Padova user on 03 November 2020

scale over which to apply M_* and SFR transformation, to produce physically meaningful measurements.

In this work, we have selected star-forming regions according to the [O I] BPT diagram. This diagram is typically capable to highlight a contribution from other physical processes rather than star formation. Mechanisms such as thermal conduction from the surrounding hot ICM and turbulence are particularly relevant for the origin of the diffuse emission (see e.g. Paper XIII). Ours is therefore a conservative choice. None the less, Appendix A shows that all the results hold also when using the [N II] diagnostic diagram.

The first result of our analysis is that, considering all galaxies together, a correlation between the $\Sigma_{\rm SFR}$ and Σ_* exists, though it is quite broad, having a scatter of 0.3 dex. The correlation gets steeper and shifts to higher Σ_* values when external spaxels are excluded from the analysis and at a given galactocentric distance moving from less to more massive galaxies. The broadness of the relation suggests galaxy-by-galaxy variations. We note that the sample includes only late-type star-forming galaxies, therefore differences cannot be driven by the morphology, as found for example by CALIFA studies (e.g. González Delgado et al. 2014). No conclusion about the role of morphology in driving the $\Sigma_{\rm SFR}$–Σ_* relation can be obtained with this sample.

The second result is that inspecting individual galaxies, each object is characterized by a distinct $\Sigma_{\rm SFR}$–Σ_* relation, indicating that no universal relation exists. Some galaxies show quite elongated sequences, some other much broader. In half of the cases the coefficient of correlation states there is no correlation between $\Sigma_{\rm SFR}$ and Σ_*, suggesting that fitting relations is meaningless. The steep slope of the global relation is therefore probably just a consequence of the different intercepts of the galaxies in the sample, which casts additional doubts on its physical meaning.

For some galaxies the scatter – if meaningful – depends on the Σ_*, for some others multisequences co-exists. The scatter of the relation does not depend on global parameters, such as total stellar mass, SFR, Δ(SFR), galaxy inclination, number of knots, SFR in the knots, SFR in the knots divided by the total stellar mass, $r_{\rm e}$.

The third result is that the broadening of the relation and the multisequences are mainly due to the presence of off-centre bright star-forming knots, that do not always follow the relation traced by the diffuse component. This result might reflect the stochasticity of the knots distribution: GMCs, that are regions where the knots form, do not follow a uniform or Gaussian distribution, but assemble and condense 'randomly' throughout the disc. SFR is not directly connected to the mass in stars in the corresponding area: indeed the mass is the integral of the star formation occurred in that region during the entire galaxy life, while star formation is the result of the ongoing gas availability.

We note that our results differ from those presented by Maragkoudakis et al. (2017). They measured the SFR and M_* of the bright off-nuclear regions and calculated the slope and dispersion of the produced $\Sigma_{\rm SFR}$–M_* relations, finding that higher surface brightness regions are not the primary drivers of the correlation for all spaxels. The discrepancy might arise from the different techniques adopted to select bright knots. Maragkoudakis et al. (2017), indeed, only focused on the 10 brightest regions on the galaxy disk of each galaxy, without applying any cut in surface brightness, as we do.

Considering the star-forming knots and diffuse component separately, we have found that the SFR in the knots is 7× higher than in the diffuse component. The radial distribution of the knots is very scattered. As a consequence, the $\Sigma_{\rm SFR}$–Σ_* relation for the knots is much broader than that of the diffuse component. The fraction of star formation happening within bound clusters (cluster formation efficiency, CFE; Bastian et al. 2012) has been investigated in a number of other single galaxies (Silva-Villa, Adamo & Bastian 2013; Adamo et al. 2015) and it has been found that it instead varies positively with both the SFR density and SFR. Galaxies with higher SFR also have on average a larger CFE (see e.g. Goddard, Bastian & Kennicutt 2010; Adamo, Östlin & Zackrisson 2011; Ryon et al. 2014). Differences might be due to the resolution scale reached by the different works.

Another important result of our analysis is that the $\Sigma_{\rm SFR}$–$\Sigma_{\rm tot\,gas}$ gas relation is as broad as the $\Sigma_{\rm SFR}$–Σ_* relation, indicating that the surface gas density is not a primary driver of the relation.

Finally, we have tried to reconcile the local $\Sigma_{\rm SFR}$–Σ_* relation to the global one, which we studied in Paper XIV. In that and in many other studies (e.g. Brinchmann et al. 2004; Salim et al. 2007; Noeske et al. 2007a, b, just to cite a few), it has been found that on global scales SFR and M_* are tightly related, suggesting that the overall current gas content is related to the current stellar mass.

We have found that the global SFMS is a continuous relation extended from the local one (see also Hsieh et al. 2017; Cano-Díaz et al. 2016), but it spans a much wider area on the plane. While on local scales the mean $\Sigma_{\rm SFR}$ and Σ_* values for all galaxies are quite similar, with mean $\Sigma_{\rm SFR}$ and Σ_* values varying of at most 0.7 dex across galaxies, regardless of the galaxy size, on global scales more extended galaxies are also more massive and more star-forming, suggesting that the SFR–M_* relation might be driven by the size–mass relation.

ACKNOWLEDGEMENTS

We thank the referee, Yago Ascasibar, for his constructive report that helped us to improve the manuscript. Based on observations collected at the European Organisation for Astronomical Research in the Southern Hemisphere under ESO programme 196.B-0578. This project has received funding from the European Research Council (ERC) under the Horizon 2020 research and innovation programme (grant agreement no. 833824). We acknowledge funding from the INAF PRIN-SKA 2017 program 1.05.01.88.04 (PI Hunt). We acknowledge financial contribution from the contract ASI-INAF n.2017-14-H.0. YJ acknowledges support from CONICYT PAI (Concurso Nacional de Inserción en la Academia 2017) No. 79170132.

REFERENCES

Abdurro'uf Masayuki A., 2017, MNRAS, 469, 2806
Abdurro'uf Masayuki A., 2018, MNRAS, 479, 5083
Abramson L. E., Kelson D. D., Dressler A., Poggianti B., Gladders M. D., Oemler A. Jr, Vulcani B., 2014, ApJ, 785, L36
Adamo A., Östlin G., Zackrisson E., 2011, MNRAS, 417, 1904
Adamo A., Kruijssen J. M. D., Bastian N., Silva-Villa E., Ryon J., 2015, MNRAS, 452, 246
Barrera-Ballesteros J. K. et al., 2018, ApJ, 852, 74
Barro G. et al., 2017, ApJ, 840, 47
Bastian N. et al., 2012, MNRAS, 419, 2606
Bigiel F., Leroy A., Walter F., Brinks E., de Blok W. J. G., Madore B., Thornley M. D., 2008, AJ, 136, 2846
Bolatto A. D. et al., 2017, ApJ, 846, 159

Downloaded from https://academic.oup.com/mnras/article/488/2/1597/5528330 by CIS Psicologia Biblioteca F.Metelli - Universita degli Studi di Padova user on 03 November 2020

Brinchmann J., Charlot S., White S. D. M., Tremonti C., Kauffmann G., Heckman T., Brinkmann J., 2004, MNRAS, 351, 1151
Bryant J. J. et al., 2015, MNRAS, 447, 2857
Bundy K. et al., 2015, ApJ, 798, 7
Cano-Díaz M. et al., 2016, ApJ, 821, L26
Cappellari M. et al., 2011, MNRAS, 413, 813
Cardelli J. A., Clayton G. C., Mathis J. S., 1989, ApJ, 345, 245
Cattaneo A., Dekel A., Devriendt J., Guiderdoni B., Blaizot J., 2006, MNRAS, 370, 1651
Chabrier G., 2003, PASP, 115, 763
Cid Fernandes R., Stasińska G., Mateus A., Vale Asari N., 2011, MNRAS, 413, 1687
Corbelli E. et al., 2012, A&A, 542, A32
Daddi E. et al., 2007, ApJ, 670, 156
Domgorgen H., Mathis J. S., 1994, ApJ, 428, 647
Elbaz D. et al., 2011, A&A, 533, A119
Ellison S. L., Sánchez S. F., Ibarra-Medel H., Antonio B., Mendel J. T., Barrera-Ballesteros J., 2018, MNRAS, 474, 2039
Erroz-Ferrer S. et al., 2019, MNRAS, 484, 5009
Faber S. M. et al., 2007, ApJ, 665, 265
Fossati M., Fumagalli M., Boselli A., Gavazzi G., Sun M., Wilman D. J., 2016, MNRAS, 455, 2028
Fritz J. et al., 2017, ApJ, 848, 132
García-Benito R. et al., 2015, A&A, 576, A135
Goddard Q. E., Bastian N., Kennicutt R. C., 2010, MNRAS, 405, 857
González Delgado R. M. et al., 2014, ApJ, 791, L16
González Delgado R. M. et al., 2016, A&A, 590, A44
Haffner L. M. et al., 2009, Rev. Mod. Phys., 81, 969
Hall C., Courteau S., Jarrett T., Cluver M., Meurer G., Carignan C., Audcent-Ross F., 2018, ApJ, 865, 154
Helfer T. T., Thornley M. D., Regan M. W., Wong T., Sheth K., Vogel S. N., Blitz L., Bock D. C.-J., 2003, ApJS, 145, 259
Hsieh B. C. et al., 2017, ApJ, 851, L24
Husemann B. et al., 2013, A&A, 549, A87
Kauffmann G. et al., 2003a, MNRAS, 341, 54
Kauffmann G. et al., 2003b, MNRAS, 346, 1055
Kennicutt R. C. Jr, 1998a, ARA&A, 36, 189
Kennicutt R. C. Jr, 1998b, ApJ, 498, 541
Kewley L. J., Heisler C. A., Dopita M. A., Lumsden S., 2001, ApJS, 132, 37
Kruijssen J. M. D., Longmore S. N., 2014, MNRAS, 439, 3239
Kumari N., Maiolino R., Belfiore F., Curti M., 2019, MNRAS, 485, 367
Leroy A. K., Walter F., Brinks E., Bigiel F., de Blok W. J. G., Madore B., Thornley M. D., 2008, AJ, 136, 2782
Lilly S. J., Carollo C. M., Pipino A., Renzini A., Peng Y., 2013, ApJ, 772, 119
Lin L. et al., 2017, ApJ, 851, 18
Liu Q., Wang E., Lin Z., Gao Y., Liu H., Berhane Teklu B., Kong X., 2018, ApJ, 857, 17
Magdis G. E. et al., 2016, MNRAS, 456, 4533
Maragkoudakis A., Zezas A., Ashby M. L. N., Willner S. P., 2017, MNRAS, 466, 1192
Mathis J. S., 1986, PASP, 98, 995
Mathis J. S., 2000, ApJ, 544, 347
McDermid R. M. et al., 2015, MNRAS, 448, 3484
Medling A. M. et al., 2018, MNRAS, 475, 5194
Morselli L., Popesso P., Cibinel A., Oesch P. A., Montes M., Atek H., Illingworth G. D., Holden B., 2019, A&A, 626, A61
Noeske K. G. et al., 2007a, ApJ, 660, L43
Noeske K. G. et al., 2007b, ApJ, 660, L47
Pan H.-A. et al., 2018, ApJ, 854, 159
Poggianti B. M. et al., 2017, ApJ, 844, 48 (Paper I)
Poggianti B. M. et al., 2019, MNRAS, 482, 4466 (Paper XIII)
Roberts M. S., Haynes M. P., 1994, ARA&A, 32, 115
Rosales-Ortega F. F., Sánchez S. F., Iglesias-Páramo J., Díaz A. I., Vílchez J. M., Bland-Hawthorn J., Husemann B., Mast D., 2012, ApJ, 756, L31
Ryon J. E. et al., 2014, AJ, 148, 33
Salim S. et al., 2007, ApJS, 173, 267
Sánchez S. F., 2013, Adv. Astron., 2013, 1
Sánchez S. F. et al., 2012, A&A, 538, A8
Sarzi M. et al., 2010, MNRAS, 402, 2187
Schiminovich D. et al., 2007, ApJS, 173, 315
Schreiber C. et al., 2015, A&A, 575, A74
Sembach K. R., Howk J. C., Ryans R. S. I., Keenan F. P., 2000, ApJ, 528, 310
Sharp R. G., Bland-Hawthorn J., 2010, ApJ, 711, 818
Silva-Villa E., Adamo A., Bastian N., 2013, MNRAS, 436, L69
Speagle J. S., Steinhardt C. L., Capak P. L., Silverman J. D., 2014, ApJS, 214, 15
Tacconi L. J. et al., 2013, ApJ, 768, 74
Viaene S. et al., 2014, A&A, 567, A71
Vulcani B., Poggianti B. M., Finn R. A., Rudnick G., Desai V., Bamford S., 2010, ApJ, 710, L1
Vulcani B. et al., 2018, ApJ, 866, L25
Vulcani B. et al., 2019, MNRAS, 487, 2278
Walter F., Brinks E., de Blok W. J. G., Bigiel F., Kennicutt R. C. Jr, Thornley M. D., Leroy A., 2008, AJ, 136, 2563
Whitaker K. E., van Dokkum P. G., Brammer G., Franx M., 2012, ApJ, 754, L29
Willett K. W. et al., 2015, MNRAS, 449, 820
Wood K., Mathis J. S., 2004, MNRAS, 353, 1126
Wood K., Hill A. S., Joung M. R., Mac Low M.-M., Benjamin R. A., Haffner L. M., Reynolds R. J., Madsen G. J., 2010, ApJ, 721, 1397
Wuyts S. et al., 2013, ApJ, 779, 135
Yan R., 2018, MNRAS, 481, 476

APPENDIX A: THE $\Sigma_{SFR}-\Sigma_*$ RELATION OBTAINED USING THE [N II]-BASED DIAGNOSTIC DIAGRAM

In the main text we have employed the diagnostic diagram based on the [O I] line ([O III]5007/Hβ versus [O I]6300/Hα) to distinguish between regions powered by star formation and regions powered by other mechanisms. In this appendix we instead adopt the [N II]-based diagnostic diagram ([O III]5007/Hβ versus [N II]6583/Hα) and show that results are robust again this choice.

To separate the regions powered by star formation, composite (SF + LINER/AGN), AGN, and LINER emission we adopt the division lines by Kauffmann et al. (2003b), Kewley et al. (2001), and Sharp & Bland-Hawthorn (2010).

Using the [N II] diagram, 142 354 spaxels are powered by star formation. The star-forming sample is therefore 1.5× larger than that discussed in the main paper. None the less, also the [N II] diagram does not detect any AGN in the sample. 99 391 spaxels belong to knots, and 42 963 belong to the diffuse component. This selection therefore slightly increases the incidence of the diffuse component. The vast majority of spaxels excluded according the [O I] diagram, but included when adopting the [N II] diagram are characterized by low values of both Σ_{SFR} and Σ_*.

Considering all galaxies together, the $\Sigma_{SFR}-\Sigma_*$ relation has a scatter of 0.35 dex, but it is qualitatively very similar to what presented in Fig. 3 (plot not shown).

Fig. A1 shows the $\Sigma_{SFR}-\Sigma_*$ relation for each galaxy of the sample separately, similarly to what shown in Fig. 4. Besides the larger number of spaxels plotted, the $\Sigma_{SFR}-\Sigma_*$ relations are very similar to the ones presented in the main text. They extend more towards lower values of both Σ_{SFR} and Σ_* values, but these stay on the same relation traced by the other spaxels.

Downloaded from https://academic.oup.com/mnras/article/488/2/1597/5528330 by CIS Psicologia Biblioteca F.Metelli - Universita degli Studi di Padova user on 03 November 2020

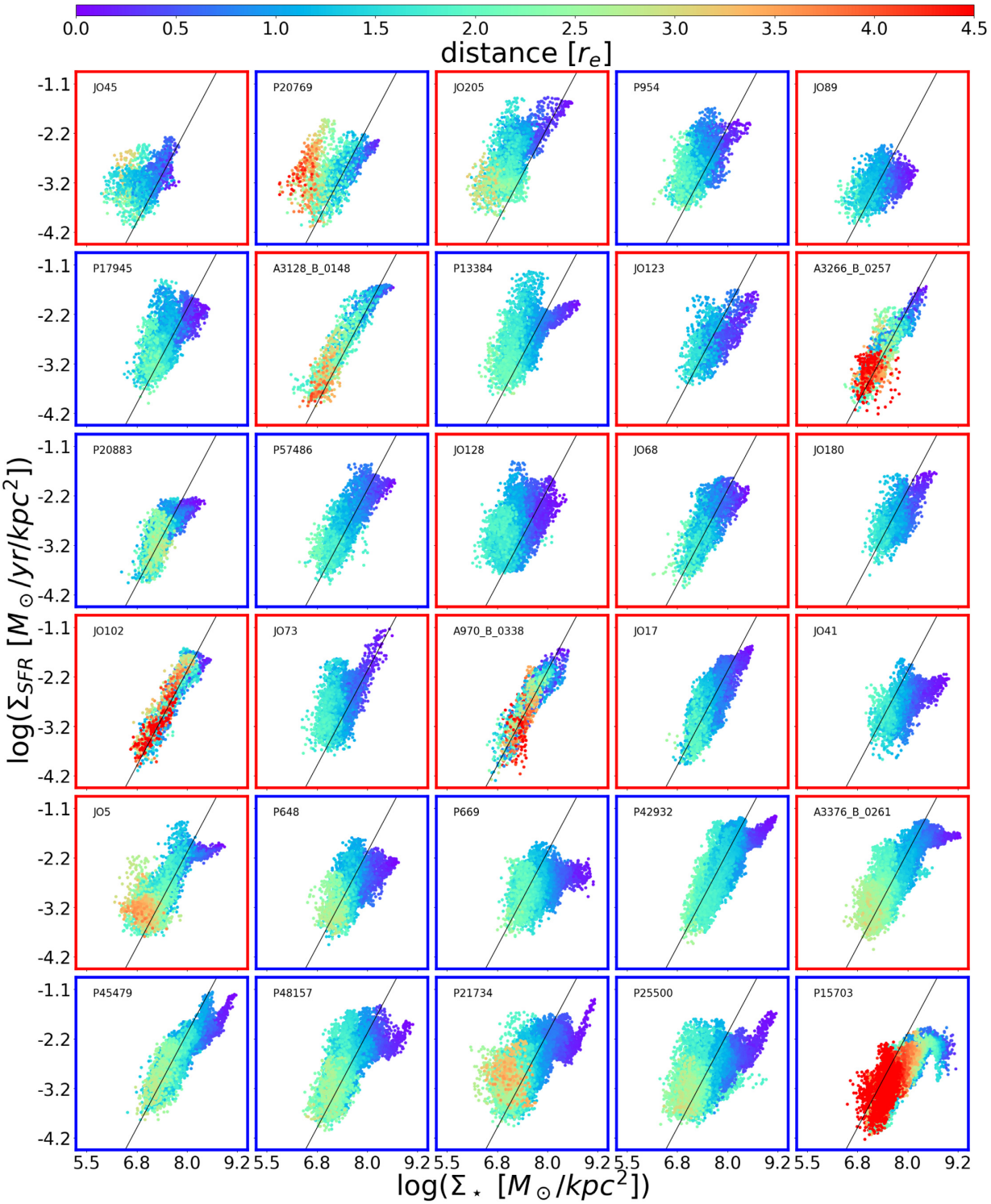

Figure A1. Σ_{SFR}–Σ_* relation for all galaxies in the sample, sorted by their stellar mass and colour coded by the galactocentric distance of each spaxel, in unit of r_e. Regions powered by star formation according to the [N II]-based diagnostic diagram are used. Galaxies surrounded by a red square belong to clusters, and galaxies surrounded by a blue square belong to the field. The black line represents the fit to the whole sample.

We have also checked that any of the results presented in the paper depends on the choice of the diagnostic diagram adopted, we can therefore conclude that the choice does not affect our findings.

APPENDIX B: THE GALAXY-BY-GALAXY VARIATION OF THE RELATION

The magnitude of the scatter of the Σ_{SFR}–Σ_* relation might depend on a number of global parameters. Fig. B1 shows this quantity

Downloaded from https://academic.oup.com/mnras/article/488/2/1597/5528330 by CIS Psicologia Biblioteca F.Metelli - Universita degli Studi di Padova user on 03 November 2020

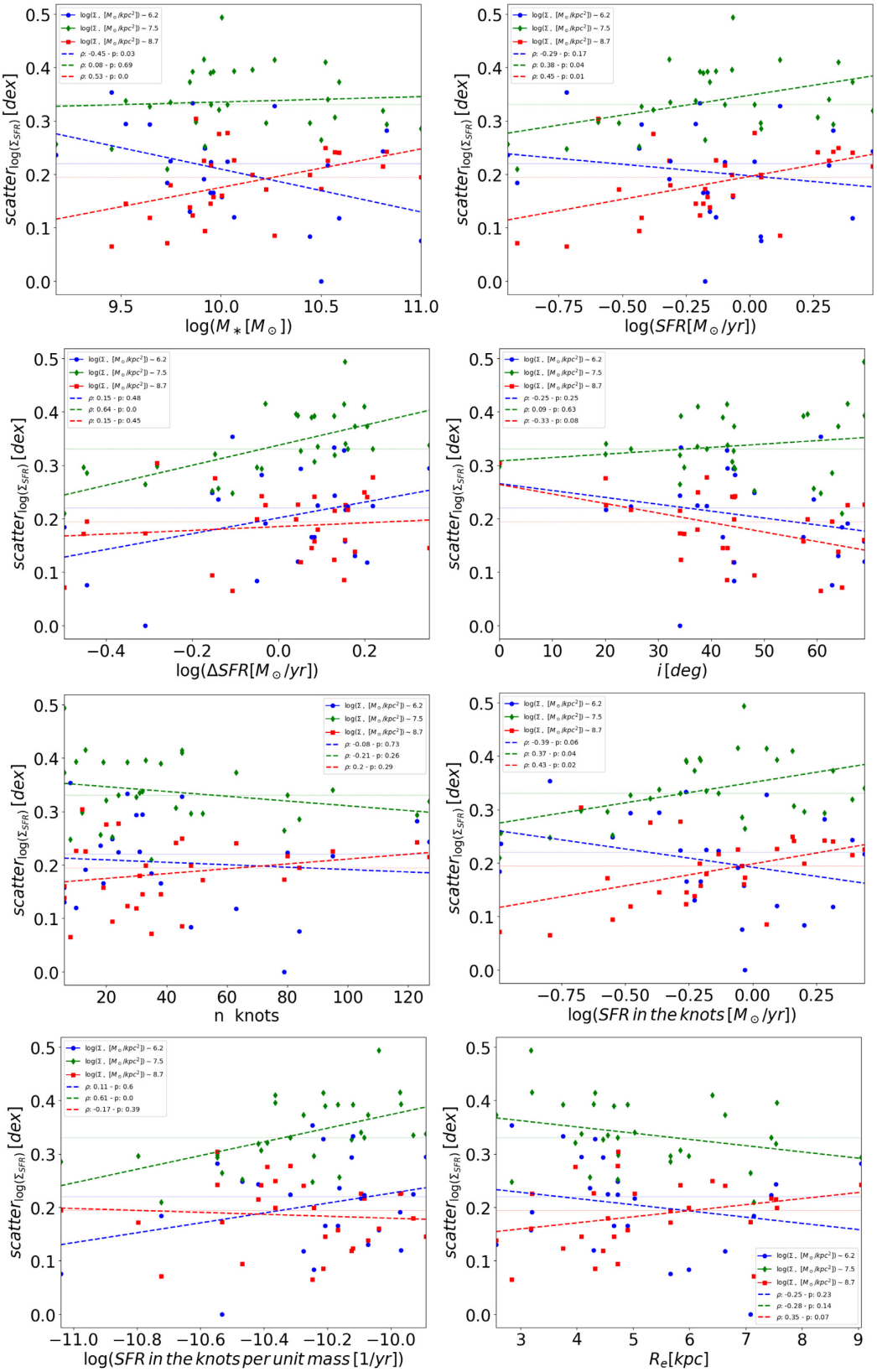

Figure B1. Scatter of the median Σ_{SFR} in three different Σ_* bins, for all galaxies in the sample, as a function of different parameters. From top to bottom, left to right: the total stellar mass, the SFR, the Δ(SFR) (see text for details), the galaxy inclination, the number of knots, the SFR in the knots, the SFR in the knots divided by the total stellar mass, the effective radius. Light horizontal lines show the median values in the three bins, dashed thick lines show the linear fits to the sets of points. In the legend, the correlation coefficients and *p*-values of the Spearman correlation test are given.

Downloaded from https://academic.oup.com/mnras/article/488/2/1597/5528330 by CIS Psicologia Biblioteca F.Metelli - Universita degli Studi di Padova user on 03 November 2020

measured in three surface mass density bins as a function of the galaxy total stellar mass, the SFR, the Δ(SFR) – i.e. the differences between the galaxy SFRs and their expected value according to the fit of the SFR–M_* relation, given their mass (Paper XIV), the galaxy inclination, the number of knots, the SFR in the knots, the SFR in the knots divided by the total stellar mass, the effective radius, respectively. We run the non-parametric Spearman test to measure the monotonicity of the relationships. The correlation coefficient varies between -1 and $+1$, with 0 implying no correlation. No strong and statistically meaningful correlations are found for any of the parameters analysed, as either the correlation coefficient ρ is close to zero or the p-value is >0.05. The only positive correlation supported by the statistical test is that with Δ(SFR) in the intermediate surface mass density bin.

This paper has been typeset from a TEX/LATEX file prepared by the author.

Downloaded from https://academic.oup.com/mnras/article/488/2/1597/5528330 by CIS Psicologia Biblioteca F.Metelli - Universita degli Studi di Padova user on 03 November 2020